

## University of Southampton Research Repository ePrints Soton

Copyright © and Moral Rights for this thesis are retained by the author and/or other copyright owners. A copy can be downloaded for personal non-commercial research or study, without prior permission or charge. This thesis cannot be reproduced or quoted extensively from without first obtaining permission in writing from the copyright holder/s. The content must not be changed in any way or sold commercially in any format or medium without the formal permission of the copyright holders.

When referring to this work, full bibliographic details including the author, title, awarding institution and date of the thesis must be given e.g.

AUTHOR (year of submission) "Full thesis title", University of Southampton, name of the University School or Department, PhD Thesis, pagination

University of Southampton  
Faculty of Physical Science and Engineering

# **Microfluidic system for chemiluminescence characterisation**

by

Ali Mosayyebi

Supervisor: Professor James S. Wilkinson

May 2013

A dissertation submitted in partial fulfilment of the degree of  
MSc Microelectronics System Design  
by examination and dissertation

## Abstract

Microfluidic technology (generally lab-on-a-chip) has been focused area of research since 90's and the main goal of this technology is to develop different chemical and biological techniques. It is quicker than the correspondent traditional techniques and consumes small volumes of material.

One of the important functions in micro scale fluidic channels is mixing that its characteristics affected by scale because the viscous forces are more than inertial forces in this range of dimensions that provides laminar flow inside the channel; in this scale the mixing is defined by diffusion rather than turbulence.

This dissertation presents the design of a microfluidic device and employing a combination of rapid prototype technology with polydimethylsiloxane (PDMS) for the fabrication. After the fabrication, chemiluminescence phenomenon is tested inside the device and the resultant images from the charge-coupled-device (CCD) camera are analysed using numerical analysis and image processing.

Two sets of tests are performed for characterising the chemiluminescence in fabricated device. Preliminary tests to check the device and the chemicals' behaviour and the actual test. In order to find the limit of detection, which is obtained as lower than  $4 \times 10^{-6}$  g of the dominant chemical (luminol) concentration in 100 ml of the solution, depends upon different parameters such as flow rate and the concentration of luminol are checked. The effect of the flow rate and the concentration on the maximum value and the decay length of the light intensity along the fluidic missing channels are then discussed.

In the final part of the project, nanoparticles are used to improve the intensity of the light in the channel in order to improve the limit of detection of the system.

## Acknowledgements

First and foremost, I thank my supervisor, Professor James Wilkinson for giving me the opportunity of working on this project and encouraging and supporting me along the way including giving access to the facility and introducing the required materials for doing the project as best as I can. In addition to his feedbacks in improving my writing.

Thanks for all members of the integrated photonics group, Dr Senthil Ganapathy, Dr. Alina Karabchevsky, Dr David Rowe, Dr Ping Hua, Mr Jonathan Butement, Mr Armen Aghajani, Mr Zilong Wang, Mr Mohd Nasir, Mr Dave Sager, Mr Neil Sessions and Mrs Jenny Morley who guided me in terms of answering my questions and sharing their ideas with me about my project, helping me with the instrumentations and facility inductions and so forth.

Thanks for Professor Hywel Morgan and all the people in his group for supports in giving me access to the bionano groups and helping me during my work.

Thanks for my tutor Professor Michael Kraft for his support during my masters education and showing me the right path in finding my interest of the future research area.

Thanks for my friend Mr Seyed Reza Sandoghchi, Mr. Mehdi Banakar, Mr. Pejwaak Salimi, Dr Ali Roghanian, Mr. Mahdiyar Sarayloo, Mr Saurabh Jain and Deepak Jain for their supports and unforgettable helps during my work.

Thanks my parent for all their supports and inspiration to do my job as best as I can.

## Table of Contents

1	Introduction.....	1
2	The aim of the project and its description.....	3
3	Microfluidics.....	3
3.1	Main flow mechanisms .....	3
3.2	Mixing in micro dimension .....	5
3.2.1	Passive.....	5
3.2.2	Active.....	6
4	Optical phenomena .....	8
4.1	Photoluminescence.....	8
4.1.1	Fluorescence .....	8
4.1.2	Phosphorescence .....	9
4.2	Chemiluminescence .....	9
5	Design, fabrication & sealing .....	10
5.1	Design.....	10
5.1.1	Shape selection.....	10
5.1.2	Device layout .....	11
5.2	Fabrication.....	12
5.2.1	Mould printing .....	12
5.2.2	Channel preparation using PDMS .....	15
5.3	Sealing.....	16
5.4	Alternative fabrication.....	18
5.5	Conclusion.....	19
6	Preliminary validation of flow system and chemiluminescence process.....	20
6.1	Velocity of micro-beads vs. syringe pump flow rate .....	20
6.2	Preparing and mixing chemicals: .....	24
6.3	Flow rate dependence:.....	25
6.4	Conclusion.....	26
7	Image and data analysis .....	27
7.1	Method 1 .....	28
7.1.1	Results for method 1:.....	28
7.2	Method 2 .....	31
7.2.1	Results for method 2:.....	35

8	Nanoparticle enhancement of chemiluminescence .....	39
8.1	Introduction .....	39
8.2	Evanescent field calculation.....	39
8.3	Approaches and results.....	42
8.4	Discussion .....	45
9	Conclusion .....	47
10	Future work.....	48
11	Reference .....	50

## Table of Figures

Figure 1: Experimental setup including optical and fluidic systems .....	2
Figure 2: (a) Laminar flow and (b) Turbulent flow [4] .....	4
Figure 3: An example of transitional flow in a branching pipe [5] .....	4
Figure 4: Jablonski diagram illustrating the process of the fluorescence, phosphorescence and chemiluminescence .....	8
Figure 5: Chemiluminescence reaction mechanisms (a) direct reaction, (b) indirect reaction [29].....	9
Figure 6: The device first design (a) as it was in the first inspiration from Guan et al. [30] work (b) as it is after the modification.....	10
Figure 7: The device 3D design using the software.....	12
Figure 8: The printed design using 3D printing machine .....	13
Figure 9: The profile of the surface measured using stylus profiler .....	13
Figure 10: The dimensions of different parts of the stylus .....	14
Figure 11: The shape of the printed channel's using optical microscope .....	14
Figure 12: 1) PDMS, 2) PDMS curing agent, 3) Beaker, 4) Scale, 5) Plastic syringes, 6) Spatula, 7) Vacuum Chamber, 8) Aluminium foil, 9) Mould, 10) Sample of wrapped mould, 11) Razor blade and needle, 12 ) PDMS channel .....	15
Figure 13: The shape of the PDMS channel using optical microscope .....	16
Figure 14: The final sealed PDMS channel .....	17
Figure 15: Some extra channels for future work .....	17
Figure 16: 3D design of the device using Autodesk Inventor, 1) top view, 2) bottom view ...	18
Figure 17: The complete printed channels using 3D printer, 1) top view, 2) bottom view .....	18
Figure 18: Velocity of the fastest particles passing from the channel centre vs. the calculated average velocity .....	21
Figure 19: COMSOL simulation results of the velocity of the particles inside the fabricated channel.....	21
Figure 20: Parabolic cross-section of the channel .....	22
Figure 21: Average points of the parabolic cross-section of the channel .....	23
Figure 22: Reynolds number vs. flow rate.....	23
Figure 23: Chemical reaction between the materials to create the required energy for exciting electrons [34] .....	24
Figure 24: The resultant light after mixing in the channels .....	25
Figure 25: An example of chemiluminescence light in the flow rate of 0.3 $\mu\text{l/s}$ in the microchannels .....	25
Figure 26: The effect of increasing the flow rate of the solution containing luminol of the concentration of 0.04 g per100 $\mu\text{l}$ of the solution of NaOH and DI Water .....	26
Figure 27: The images arrangements used for analysing them.....	27
Figure 28: A box covering the setup.....	28
Figure 29: Flowchart of the first method for each concentration and flow rate .....	28
Figure 30: The intensity of light in different concentrations .....	29
Figure 31: The effect of the flow rate on total intensity of the light.....	30
Figure 32: A predefined pattern covering the channel.....	31

Figure 33: The demonstration of the idea at the back of having a pattern over the channel ...	31
Figure 34: The flowchart for the code which has used the red pattern over the channel .....	32
Figure 35: An image by the lines introduced to get the maximum points of the intensity, a) 2D view of the image, b) 3D view of the image (MATLAB) .....	33
Figure 36: a) intensity along one of the lines, b) finding the best fit for the intensity and removing the noises, c) finding the maximums and alternatively middle pints which has been illustrated by blue circles (MATLAB).....	33
Figure 37: Using two blues circle points and draw the red line between them (MATLAB)...	33
Figure 38: Demonstration of the introduction of an origin for each image .....	34
Figure 39: Pattern on top of the image.....	34
Figure 40: Average figure plotted having 20 separate figures for the concentration of 0.008 g luminol in the flow rate of 0.3 $\mu$ l/s.....	35
Figure 41: The intensity of the light in different concentration of luminol .....	36
Figure 42: Flow rate effect on the intensity of the light along the channel .....	36
Figure 43: Movement of the peaks by increasing the flow rate.....	37
Figure 44: Distance from the maximum of the light intensity peak .....	38
Figure 45: Picture related to Table 4.....	41
Figure 46: Average intensity over the different concentration of luminol to find limit of detection.....	43
Figure 47: The average pixel intensity of chemiluminescence without nanoparticles (DI water) and with nanoparticles (20 nm Au and Ag) .....	45
Figure 48: Future device layouts including "light source" and "optical amplifier" parts .....	48



## 1 Introduction

Challenges in lab-on-a-chip devices in terms of having greater multi-functionality such as operation and recognition of bacteria, protein and DNAs etc., in just a small device is interesting and challenging in academia and laboratories in the globe.

Calcium plays many important roles in human biology, including bone and tooth structure, helping enzymes work properly in terms of producing energy from foods, repairing DNA etc., muscle function and also cell signalling. Detecting the concentration of calcium inside the human body is an issue. In 1962 Osamu Shimomura discovered then the reaction between photoprotein aequorin and calcium ions results in bioluminescent emission allowing detection of calcium in the liquid [1].

Microfluidic channels are suitable for characterising luminescence reactions for several reasons:

- a. The flow of fluid through channels of micron-scale cross-sections is typically laminar. Such layered behaviour means that analysing fluid behaviour is simpler than turbulent flow usually encountered at the macroscale.
- b. In microfluidic channels, sample consumption is reduced compared to traditional fluid handling techniques such as test tubes.
- c. Microfluidic test devices can have very small footprints.

The purpose of this project is to produce an optically characterised microfluidic device using a rapid prototype technique. This device will be employed for future work in order to detect calcium ions in unknown liquids using aequorin. The bio prefix of 'bioluminescence' signifies the biological mechanism of light emission.

Instead of bioluminescence, the characterisation of the device in this project will be done using chemiluminescence (which is a chemical rather than biological effect) for the following reasons:

- a. Aequorin is not immediately available.
- b. Dealing with biological materials always raises more potential hazards and limits the places they can be used.
- c. The required materials for chemiluminescence are easier to find.
- d. The hazards for using these chemicals are fewer than those for biological materials.

The 3D printing prototype technique that is used in this project includes laying out the 3D design of the device in a computer-aid design (CAD) tool, loading it into the 3D printer's system and converting it into discrete layers, where the layers have specific thicknesses that correspond to the machine printing limitation.

The optical system used in this experiment includes an optical microscope, objective lens and high speed camera in addition to the fluidics instrumentation. The overall view of the setup is

## Introduction

shown in Figure 1. The lens has a confocal length of 8 mm and a maximum aperture size of  $f/1.4$ . The camera used was the Hamamatsu ORCA – R<sup>2</sup>, with 1.3 megapixel cooled interline sensor and a frame rate of 16 frame per second (fps) at its maximum resolution. There are two fluid mixtures used in the experiment which are pumped into the inlets using syringe pumps 1 and 2.

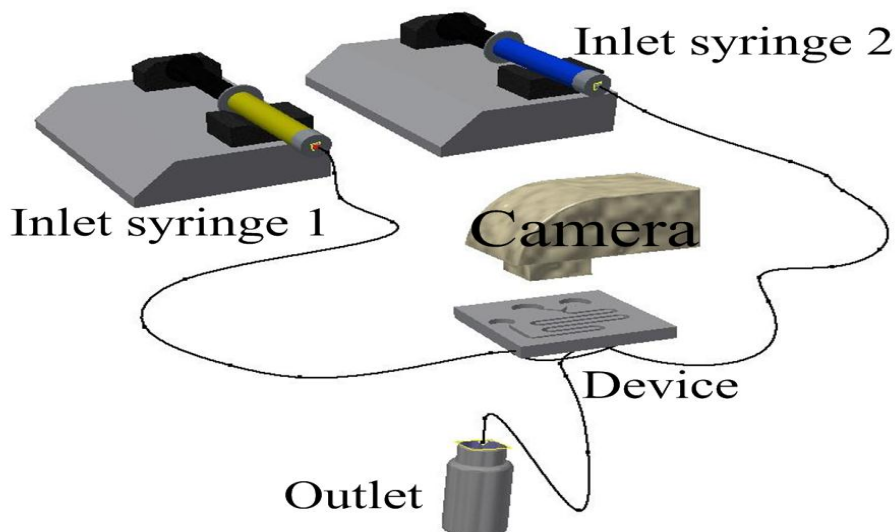


Figure 1: Experimental setup including optical and fluidic systems

The resultant images are analysed using two analysing schemes. First, integrating values of all pixels over a predefined area, which covers the whole length of channel. The result will allow finding the limit of detection (LoD) for the luminol. Second, fitting a pattern over the design to measure the intensity along defined lines crossing the channels and the result will describe the effect of the luminol concentration and also its flow rate change, in one of the inlets, on light decay length along the channel.

In the final part of the project, it is investigated whether the intensity of emitted light and hence detection limit can be improved by using gold nanoparticles. Specifically, it may be possible to exploit their surface plasmon properties to localise the light intensity around them during the chemiluminescence experiment.

After designing, fabricating and characterising the microfluidic channel, setting up the experimental instrumentation and characterising the chemiluminescence, the system is ready for aequorin and calcium ions to be mixed inside the channels to determine calcium concentration by bioluminescence. This will be the next stage of the project to be undertaken by other researcher once the protein chemistry is established.

## 2 The aim of the project and its description

The aim of this project is to fabricate a new microfluidic device for a chemiluminescence (CL) assay. The project involves using syringe pumps to drive the fluids through a chip whilst measuring the emitted CL. This will allow determination of the lowest concentration that can be detected with the available optical instrumentation. Using a different analytical scheme for analysing the images, the decay length of the CL light will be determined with respect to flow rate and chemical concentration. Finally, the system will be used to assess whether spherical gold and silver nanoparticles can cause a reduction in the limit of detection (LoD).

## 3 Microfluidics

To mix chemicals faster, with less fluid consumption and greater control, a microfluidic device is chosen. Other reasons for using microfluidics are:

- a. Cheaper mass production compare to the traditional process such as photolithography, milling etc.
- b. More comfortable usage compare to the traditional way
- c. Portability compare to the processes at which lots of equipment required
- d. Faster analysis compared to the traditional way

This chapter describes the main fluid flow mechanisms, different types of microfluidic mixing devices and luminescent emission.

### 3.1 Main flow mechanisms

In 1880, Osborne Reynolds described a relationship between inertial and viscous forces in a fluidic channel and presented an equation to distinguish between different regimes of flow behaviour [2]. In this section a brief description of different fluid flow regimes according to their corresponding Reynolds number is presented [3].

The Reynolds number,  $Re$ , is defined as:

$$Re = \frac{v \cdot \rho}{\mu \cdot L} \quad \text{Equation 1}$$

where  $v$  is fluid flow velocity,  $\rho$  is fluid density,  $\mu$  is fluid viscosity and  $L$  is tube length.

There are two main flow regimes:

- a. Laminar flow, which refers to the apparent structure, composed of thin layers. Laminar flow indicates multiple streamlines of fluids sliding over each other without intersection (Figure 2(a)).
- b. Turbulent flow, where the streamlines of fluid intersect due to small chaotic vortices, which mix the flow and cause the mathematical simulation complexity (Figure 2(b)).

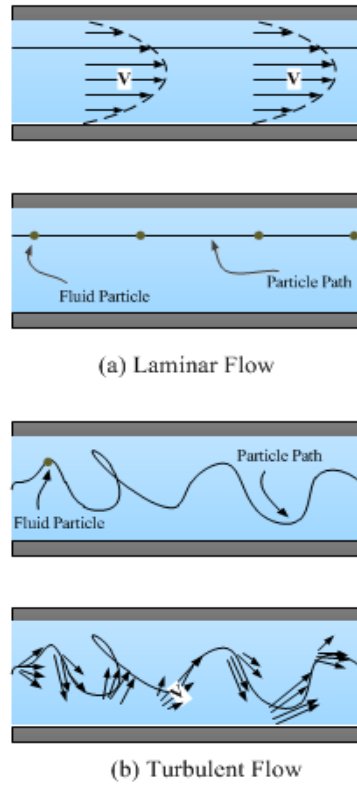


Figure 2: (a) Laminar flow and (b) Turbulent flow [4]

There is an intermediate state between laminar and turbulent flow called transitional flow. Figure 3 shows an example of this type of flow in a branching pipe.

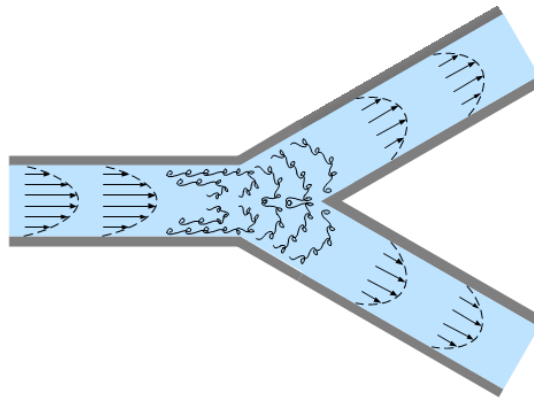


Figure 3: An example of transitional flow in a branching pipe [5]

The following bullet points show the approximate relations between different flow regimes and their corresponding Reynolds numbers:

- Laminar: inertial force  $\gg$  viscous force,  $Re \ll 2100$
- Turbulent: inertial force  $\gg$  viscous force,  $Re \gg 4000$
- Transitional: inertial force  $\approx$  viscous force,  $2100 \ll Re \ll 4000$

Typically, diffusion is the only way that mixing can happen in laminar flow. The mixing rate will be increased by introducing bends along a channel. Dean vortices cause lateral flow as a result of the channel bends. The Dean number  $De$  is a dimensionless parameter that quantifies such behaviour and is related to the Reynolds number by the curvature radius and channel diameter, as given in Equation 2 [6]:

$$De = Re \sqrt{\frac{D}{2R}} \quad \text{Equation 2}$$

$D$  is the width and  $R$  is the radius of curvature. The higher the Dean number is, the better the mixing will be, as an example in Hessel et al. work for four vortices  $De > 140$  [7].

## 3.2 Mixing in micro dimension

Mixing in laminar flows is dominated by diffusion, which is an inherently slow process and requires excessively long channels for complete mixing. The length of a microfluidic circuit can be reduced by increasing the rate of mixing. Different shapes, designs and techniques of mixing are being used in research laboratories in the last few years [7]. In this section, the main two different types of micromixers, active and passive micromixers, are described and compared. The main point in distinguishing active micromixers from passive micromixers is their requirement for an external energy source.

### 3.2.1 Passive

This type of micromixer is recognized for its simplicity because it does not use an external source. On the other hand, the lack of external source requires a different design procedure to improve diffusive mixing. In this section, several types of micro-mixer are described.

#### 3.2.1.1 Parallel and serial lamination micro-mixers

This type of mixer uses  $n$  sub-streams of inlets, which results in the reduction of path length and the increase of interaction surface enhancement and provides simpler and quicker mixing than a long, straight channel.

The main designs of this type are called “T” and “Y” mixers and researchers have tried to achieve better mixing by modifying them. For instance, Andrew G. Hadd [8] and his colleagues in Tennessee in 1997 obtained the Reynolds number of about 0.014 using a T-mixer fabricated on glass. Two years later, Veenstra et al. [9] in Netherland, used silicon-glass to fabricate their channel to increase the Reynolds number to 0.023. Another group in Washington [10] used the same material to achieve the Reynolds number of 0.3. The last example is the work of M. Al-Rawashdeh et al. [11], who fabricated micro- and millichannels to form T-mixers that reached the Reynolds number of about 500.

There have been several examples of Y-mixers, which have used different materials and achieved different Reynolds number. Ismagilov et al. [12] used polydimethylsiloxane (PDMS) to get the Reynolds number of about 0.4. In 2004 Wu et al. [13], in Singapore reached the Reynolds number of about 0.02 using a channel fabricated in polymethylmethacrylate

(PMMA). Finally in 2012 Wang et al. [14] employed PDMS with circular holes through the channel in order to increase the Reynolds number to 100.

There are special types of parallel lamination called “injection micromixers”, which use plumes in one of the inlets as in the work of Shakhawat Hossein et al. [15]. This work contained a numerical study of zigzag, square wave and curved channels and succeeded in getting the Reynolds number of about 260.

The inspiration of design of the current project is coming from this type of passive micromixers and specifically y-shape channels and the reason is the simplicity of the design which provide a reasonable mixing.

### **3.2.1.2 Chaotic advection**

The concept of this type of mixer is finding a channel in which the flow is split, stretched, folded and broken. Quantitative comparisons of this type of mixer are beyond the scope of this report, so this section will instead focus on the qualitative mixing properties of chaotic advection.

Wang et al. in 2002 [16] studied the theoretical behaviour of a mixing channel with obstacles in the channel. They showed that by using different placements of obstacles inside the channel, the lateral mass transfer could be achieved.

### **3.2.1.3 Droplet micromixers**

In this type of device, mixing is obtained solely by droplet movement and better mixing would be achieved well defined flow patterns in each part that causes rapid mixing segment flow. To find more information about this technique, Hosokawa K et al. [17], Paik P et al. [18], Michael D. et al [19], Zhi-Xiao Guo et al. [20] and [21] could be mentioned as some examples.

In conclusion, three main types of passive micromixers are described. The simplicity of Y-shape micromixer technique makes it particularly well suited to this project.

## **3.2.2 Active**

Active micromixers require external sources to provide the energy required to mix fluids and as such can be categorised by their external sources. Several different types of active micromixers are mentioned below.

### **3.2.2.1 Dielectrophoresis**

Dielectrophoretic mixing is a chaotic process where polarised particles are manipulated by an applied electric field. For example, Campisi et al. [22] have demonstrated this type of mixing.

### **3.2.2.2 Thermal actuation**

Thermal actuators are MEMS devices that use thermal changes and transform them into the motion. As an example, Xue et al. [23] studied the mixing of two miscible fluids inside a T-shape channel made in PMMA and reduced the mixing length, which starts from the inlets junction to the position along the channel where the light is decayed, to 6000  $\mu\text{m}$ .

### 3.2.2.3 Magnetohydrodynamic flow

The interaction of magnetic fields and moving electrically conducting fluid is the basis of magnetohydrodynamic flow (MHF), which is a method in microbiological assays. [24]. As an example, researchers in the University of Akron and Washington State University [25] used magnetic micromixers to reach a mixing time of 1100 ms and a mixing length of 500  $\mu\text{m}$ .

There are other types of active micromixers such as: acoustic, electrokinetic, pressure disturbance, electrohydrodynamic etc. and could be found in [26] and [7].

In summary, different types of active and passive micromixers are described and some of the examples of are given. They passive Y-shape micromixer will be used in this report for its simplicity and lack of external source.

## 4 Optical phenomena

This chapter discusses the optical phenomena investigated in this project.

Any visible incident that is the result of light and matter interacting is called an optical phenomenon [27]. Luminescence is an important optical phenomenon that could be divided into different categories with respect to the duration of the light and the source producing the light in the process.

Photoluminescence and chemiluminescence are two of the main types of luminescence and are described below.

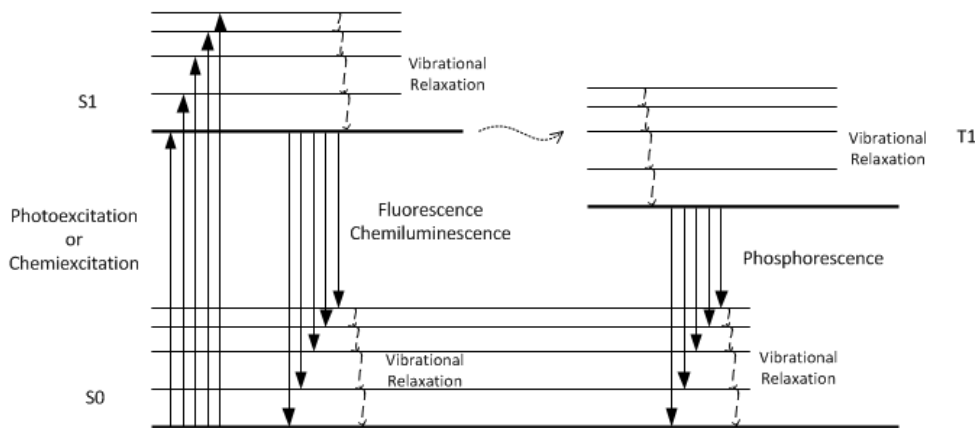


Figure 4: Jablonski diagram illustrating the process of the fluorescence, phosphorescence and chemiluminescence

### 4.1 Photoluminescence

Photoluminescence is a type of luminescence light involving electromagnetic excitation energy (photons) and radiated photons. There are two main types of photoluminescence (fluorescence and phosphorescence), which are shown in Figure 4 and described below.

#### 4.1.1 Fluorescence

Fluorescence or rapid photoluminescence is the process in which electromagnetic energy causes electrons to jump into an excited state and a photon is emitted as they relax to the ground state. This process takes about  $10^{-8}$  s. The process includes:

- 1) Exciting the electrons located in the lowest vibrational level of the ground state into a higher energy vibrational state, which takes about  $10^{-15}$  s.
- 2) Returning the excited electron to the lowest vibrational state of the excited state by passing the process of vibrational Relaxation through the vibrational states and singlet states, in which most of the energy will transfer to heat.
- 3) Returning the electron from the lowest vibrational state of the excited state to the ground state and radiating a photon in the process. The wavelength of the emitted photon is a function of the difference between the ground and excited states (fluorescence). The electrons may jump directly to the lowest singlet state energy level or again jump to the excited



vibrational state located in the ground state and then, by passing through the vibrational relaxation and transforming the energy to heat, they reach to the lowest vibrational level of energy, which will take about  $10^{-8}$  s. This description could be found inside the diagram shown in Figure 4.

### 4.1.2 Phosphorescence

This process is similar to fluorescence. The only difference is in the third step where in fluorescence, electrons jump back from the excited singlet state directly to the lower singlet state located in the destination energy level, whereas in phosphorescence, electrons jump to the lower excited singlet or triplet states first and then jump back to the ground singlet state. Having more steps to pass as it is shown in Figure 4 through makes this process take longer ( $10^{-4}$  to  $10^4$  s).

## 4.2 Chemiluminescence

Chemiluminescence, the optical phenomenon used in this project, is similar to photoluminescence except the excitation source for chemiluminescence is the energy produced by an exothermic chemical reaction whereas for photoluminescence it is a photon. The chemiluminescence produced by biological organisms called bioluminescence [28].

In general, chemiluminescence can be separated into a direct and an indirect reaction. The direct reaction is the process the chemical energy is equal to  $h\nu$  required for exciting the electron. The indirect reaction relates to molecules that require more steps for producing light where the energy of the excited state transfers to the fluorophore after which there will be some  $h\nu$  resultant energy. This effect is shown in Figure 5.

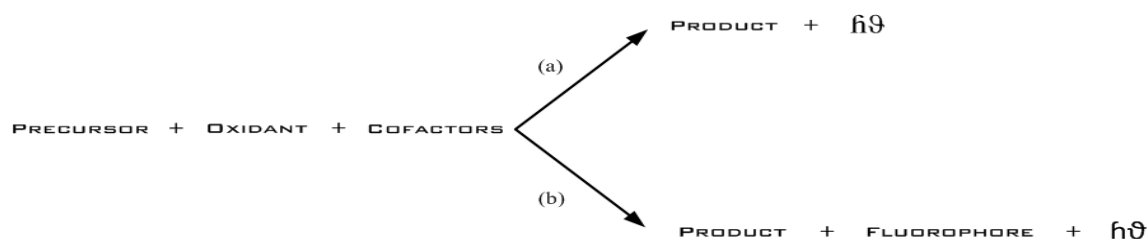


Figure 5: Chemiluminescence reaction mechanisms (a) direct reaction, (b) indirect reaction [29]

Reviewing the phenomena explained above, chemiluminescence has the advantages of:

1. Not requiring an external light source,
2. The intensity of the light can be easily controlled by the concentration of the analyte.

Therefore, the project will use that as the reaction to be tested inside channels.

In conclusion, two main types of luminescence phenomena are explained. The controllability and availability of chemiluminescence reagents are advantages compared with bioluminescence for demonstrating mixing inside a microfluidic channel.

## 5 Design, fabrication & sealing

This chapter describes the design and fabrication of the microfluidic device for chemiluminescence characterisation, from the point of the design's first inspiration to the point at which it is tested as the actual device. The design section includes the steps for finalising the shape and also using the software to do its layout. The fabrication section includes using the 3D printer to print the layout, then using polydimethylsiloxane (PDMS) to make the channel from the mould and seal the device.

### 5.1 Design

This part includes two sections: 1) the first inspiration and choice of design, 2) the software used for designing the device.

#### 5.1.1 Shape selection

Prior to fabrication, the device was designed using Autodesk Inventor Pro 2013 software to fit the following:

- 1) The 3D printing process,
- 2) The available fabrication facilities in the University of Southampton.

The shape of the channel (depicted in Figure 6(a)) was inspired by the working Guan et al. [30].

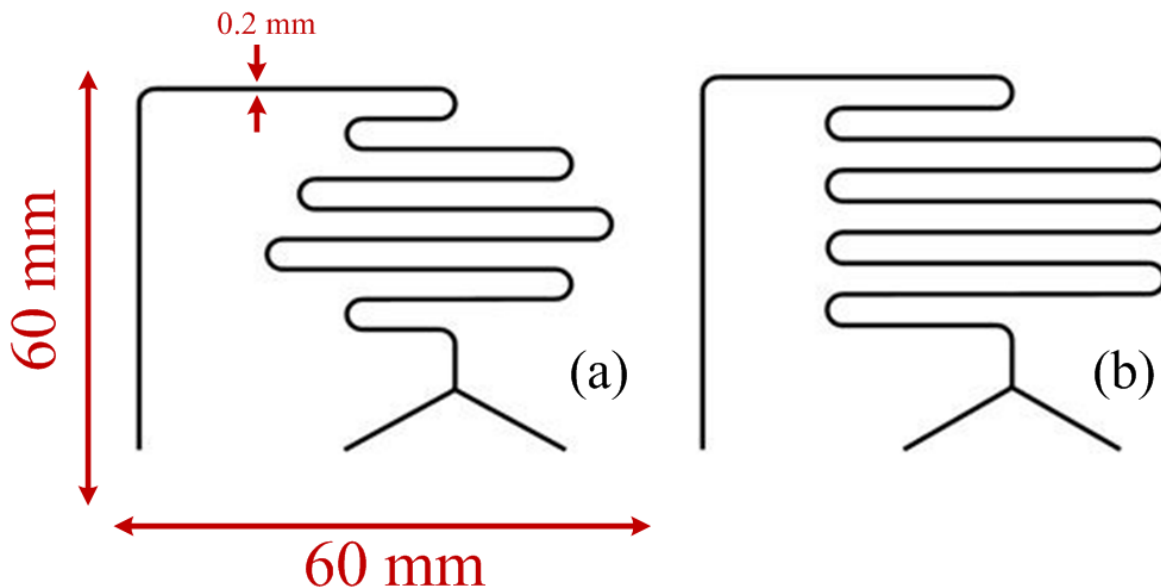


Figure 6: The device first design (a) as it was in the first inspiration from Guan et al. [30] work (b) as it is after the modification

The design depicted by Guan et al. had the following advantages:

- 1) Managing a long channel in a small area,

- 2) Having bends in the design, which improves mixing (bends long the channel provide dean flow, which provide better mixing).

The design is slightly changed in this project in order to have a longer channel, as shown in Figure 6(b). Additionally, the resolution of Z axis of the printing machine is  $32\text{ }\mu\text{m}$ , which means that the dimensions of the printed device should be an integer multiple of this value. Moreover, a reasonable number of the investigated mixing channels described in the literature have a width of about  $100\text{ }\mu\text{m}$  to  $200\text{ }\mu\text{m}$  [26] [7]. Having these in mind as well as considering the low Reynolds number, which includes the diameter of the channel, the width and the length of the channel cross-section were chosen to be  $200\text{ }\mu\text{m}$ . Furthermore, this size of the channel is helpful in terms of having sufficient chemiluminescence light because decreasing this dimension will lower the signal to noise ratio because the amount of the light inside the channel will decrease and analysing the resultant images will be more challenging.

As a conclusion, in this section the decision about the shape and the dimension of the channel is made. For simplicity, the depth of the channel is taken equal to the width of  $200\text{ }\mu\text{m}$ .

### 5.1.2 Device layout

This section describes the details of layout, the software that is used and finally the layout.

The software that is employed to layout the device is Autodesk Inventor Pro 2013. Table 1 summarises some of the more common parts of the software.

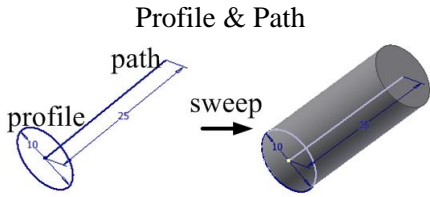
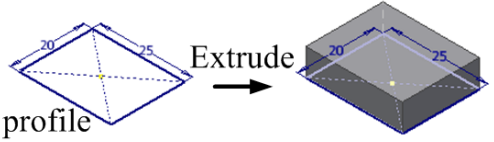
	Sweep	Extrude
<b>Requirements</b>		
<b>Explanation</b>	Using a profile and a path passing through to draw a uniform channels and tubes	Using a profile and extruding to the values of the interest in order to have a box
<b>Usefulness</b>	It is easy to layout the channel	Useful to layout the base of the design which is just a box with few millimetre thickness
<b>Challenges</b>	Having a junction of the channel using just one profile is not easy and in order to have a uniform and same width and depth in each branches of the junction, introducing separate profiles required	Since it requires just profile, then layout a channel with different depth along the channel using this tool is not easy

Table 1: The summary of the main tools used in the software to layout the device sketch

Figure 7 is showing the device which has been layout using the software; the black area is the channel and the grey area is the substrate.

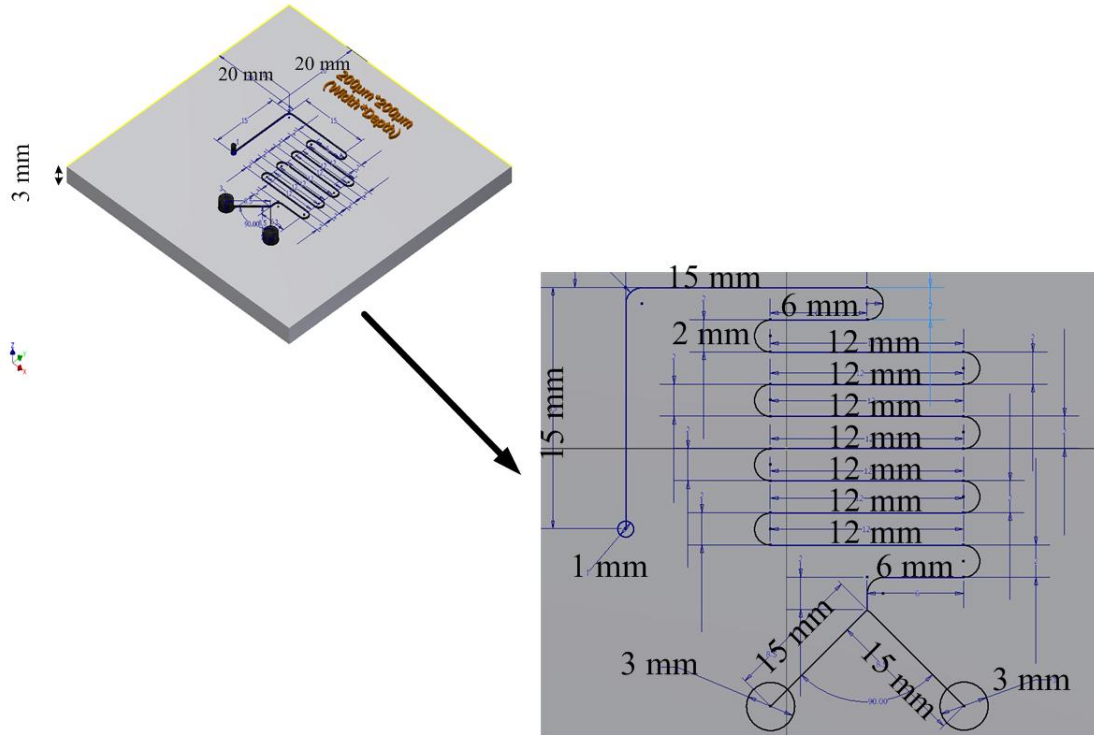


Figure 7: The device 3D design using the software

As a conclusion, the appropriate shape and diameters of the channels have been selected and using the software and also using the specification, which is mentioned in the previous section, the device is designed and the layout is done and saved in stereolithography (STL) format, which is the defined format recognised by fabrication machine.

## 5.2 Fabrication

In this part the device is fabricated. This section includes: printing a mould, using PDMS to make the channel and seal the channels using oxygen plasma.

The flexibility of PDMS after it is cured and turned to a thick elastic semi-solid material made it as one of the best choices for making the channels. This turns out to be more obvious after using the oxygen plasma to seal the device in which using a slight pressure, PDMS sticks to the glass surface and the surfaces which are not completely flat are covered by the PDMS.

### 5.2.1 Mould printing

This section describes 3D printing and using this technology to print the mould of the design. Also some specifications such as the resolution of the machine, which have a direct effect on the design, are mentioned here.

Using 3D printing for printing the whole device in one goes is discussed in the “5.4 Alternative fabrication” part.

Although the specification of the machine states that it can print layers of 16  $\mu\text{m}$ , it was found that the resolution of the device in the best condition is 32  $\mu\text{m}$  thickness for each layer.

The process involves:

- Loading the stereolithography (STL) format of the design
- The machine software splits the design to layers with  $32\text{ }\mu\text{m}$  thickness
- The machine uses pins that put the UV-cured polymer (Tango) on top of each other to print layers.

Figure 8 shows the final shape of the device after being printed in the machine. The two big circles in the figure are input reservoirs and the small one is the output reservoir.

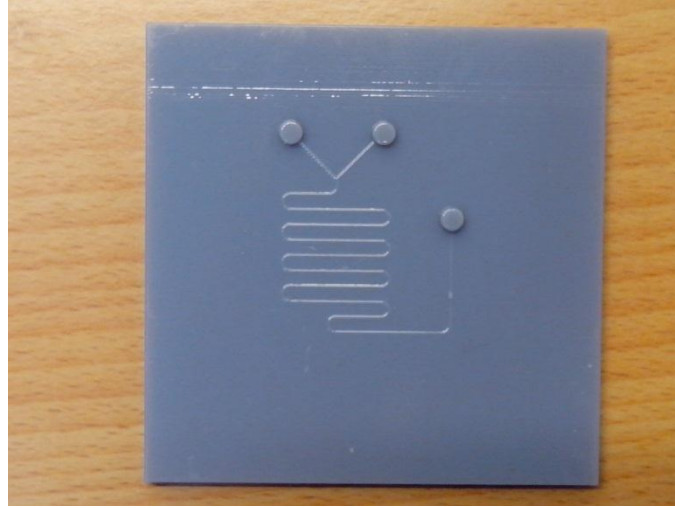


Figure 8: The printed design using 3D printing machine

The stylus profiler is used to check the channel depth, roughness of the surface and the accuracy of the device in terms of its shape.

Figure 9 shows the result of stylus profiler in which the height of the channel is measured  $180 \pm 7\text{ }\mu\text{m}$ .

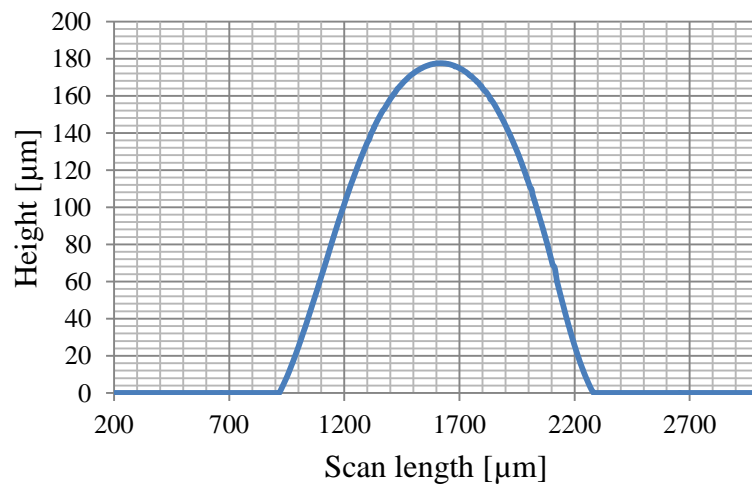


Figure 9: The profile of the surface measured using stylus profiler

Stylus profiler is based on the vertical movement of the needle which moves across the surface and scans. Since the tip of the profiler has an angle of  $60^\circ$ , it cannot resolve sample features with a greater angle. The profiler also cannot resolve wells or dips narrower than the stylus width. When a feature is too steep but not too narrow to be characterised, the profiler can still be used to measure its relative height. Figure 10 illustrates this explanation in a clearer manner.

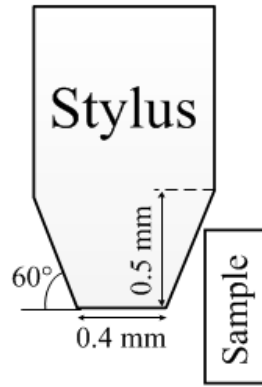


Figure 10: The dimensions of different parts of the stylus

Figure 11 demonstrates the shape of the device using an optical microscope.

An alternative way of seeing the surface of the device, which could be suggested for future work, is scanning-electron-microscope (SEM) that has better resolution of several nanometres. Since the material of the device is a nonconductive polymer, it would have to be coated by metal e.g. gold in order to be used sufficiently in the microscope.

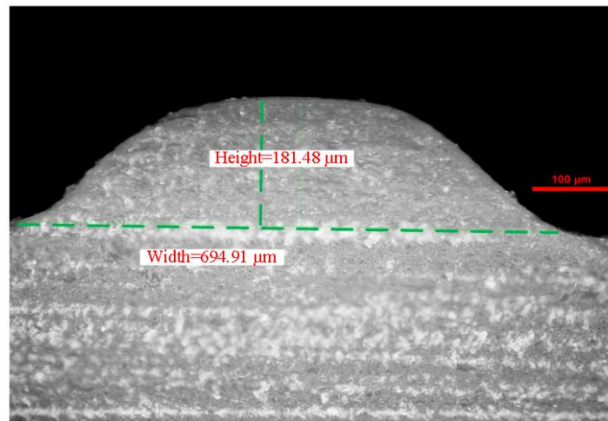


Figure 11: The shape of the printed channel's using optical microscope

The manufacturer of the 3D printing machine states that it has a vertical resolution of  $16\ \mu\text{m}$  but using the machine for a long period has decreased the resolution: the height of the channel mould cannot be less than  $\sim 30\ \mu\text{m}$ . The y and x resolution looks worse in terms of well-defined printing. Figure 11 shows a semi-elliptical shape with a width of  $\sim 700\ \mu\text{m}$  whereas it was supposed to have a square cross-section with a width of  $200\ \mu\text{m}$ .

In conclusion, 3D printing machine was used to print the microfluidic channel mould designed in “5.1.2 Device layout”. This will be used for making channels using PDMS.

### 5.2.2 Channel preparation using PDMS

In this section, channels are made by pouring PDMS on top of the printed mould.

In order to have well-defined PDMS channels that don't adhere to the printed device, the mould needs to be non-adhesive. There are different ways of making this happen such as covering the surface of the mould with some chemical to affect contact angle. However, such chemicals are usually dangerous. The easiest way to increase hydrophobicity is to leave the mould inside an oven at 90 °C for one hour. This is temperature as to be below 100 °C so that the mould doesn't melt.

After preparing the hydrophobic mould, the following steps are followed to get the final channel:

- a. Preparing the PDMS:
  - i. Vigorously mix PDMS with its reagent by the ratio of 10:1 by mass respectively
  - ii. Put the mixture inside the vacuum chamber and leave in the fridge for an hour until the bubbles disappear
- b. Wrap the mould with aluminium foil and form walls around it to contain the PDMS
- c. Pour PDMS on top of the wrapped mould
- d. Put the PDMS-filled mould inside the oven at 100 °C and leave it for at least an hour
- e. Take it out of the oven and leave it for couple of minutes to be cooled
- f. Cut the aluminium foil surrounding the PDMS carefully and take off the cured semi-solid PDMS channel from the top of the design

Figure 12 shows the materials and the tools used to make the PDMS channel.

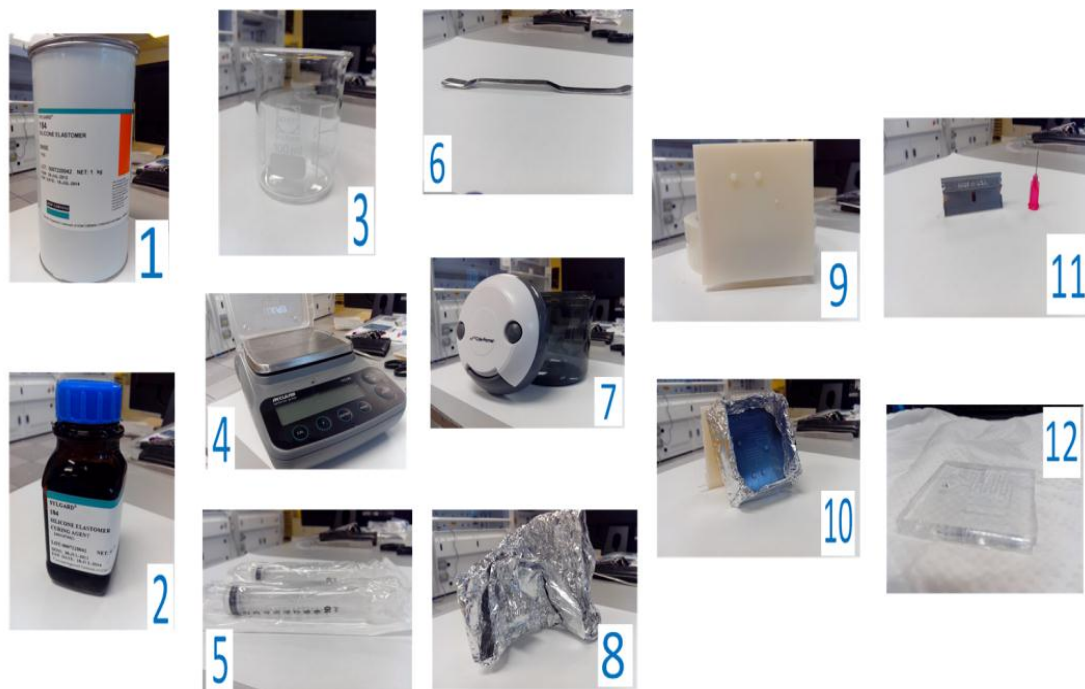


Figure 12: 1) PDMS, 2) PDMS curing agent, 3) Beaker, 4) Scale, 5) Plastic syringes, 6) Spatula, 7) Vacuum Chamber, 8) Aluminium foil, 9) Mould, 10) Sample of wrapped mould, 11) Razor blade and needle, 12) PDMS channel



Figure 13 shows the shape of the PDMS channel using optical microscope. The PDMS maintains the same shape as the mould. The differences between the width of the mould and the width of PDMS channel are because the temperature used for curing PDMS makes the channels shrink slightly. The PDMS channel is going to be sealed in the next section.

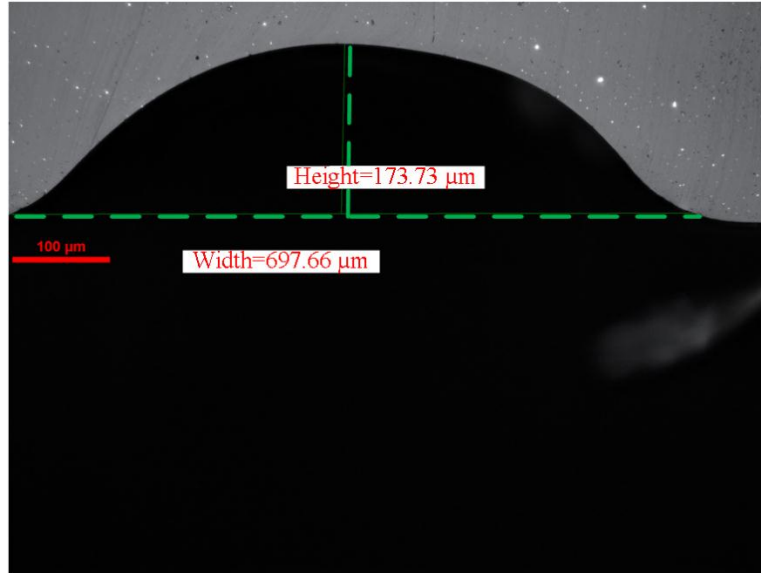


Figure 13: The shape of the PDMS channel using optical microscope

### 5.3 Sealing

The channels prepared in the last section are open from top. In order to cover the top of the design one of the best choices is to attach it to a glass slide. The transparency of the glass will not block the researcher's view.

One of the options that could be used to bond the PDMS channel to the glass is the reactive ion etcher (RIE). Plasma treatment on each of the two contacting surfaces will provide a strong permanent bond between them when pressed together.

The operating method of RIE is using a powerful Radio Frequency (RF) field to ionise oxygen molecules and create a plasma on the surfaces inside the chamber [31] [32]. The specifications of the machine are in Table 2:

Parameter	Chamber Pressure	Treatment Duration	RF Power	Base Pressure
Value	200 mtorr	20 s	20 W	$1 \times 10^{-5}$ torr

Table 2: RIE specification

Figure 14 shows the final sealed PDMS channel.



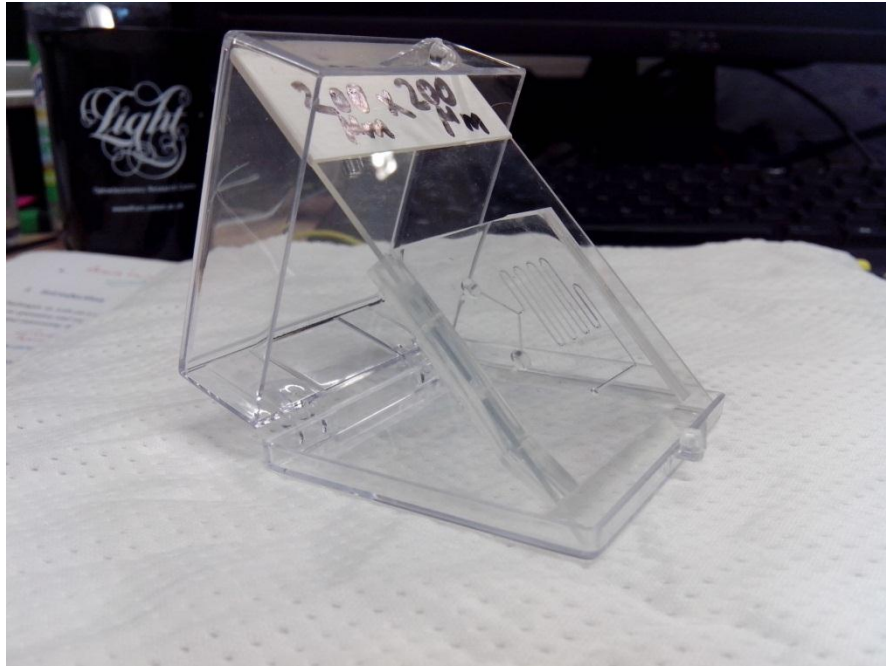


Figure 14: The final sealed PDMS channel

As a conclusion, the PDMS channel of the last section is permanently sealed to a glass slide using RIE and the result is shown in Figure 14.



Figure 15: Some extra channels for future work

In summary of the whole design, fabrication and sealing, the design of the channel, in terms of choosing the appropriate shape and to layout in software, is finished; also the fabrication of the mould using 3D printer is done and this fabricated device employed as a mould to be used for preparing a PDMS channel and finally the channel is sealed to a glass slide using RIE.

Figure 15 shows some of the alternative designs using the same process which could be used in future works.

#### 5.4 Alternative fabrication

This section discusses less successful processes, which might help future researchers use their time and energy more usefully.

One idea was to print the whole microfluidic circuit at once using 3D printing, as shown in Figure 17. The design of the device in Autodesk Inventor is illustrated in Figure 16.

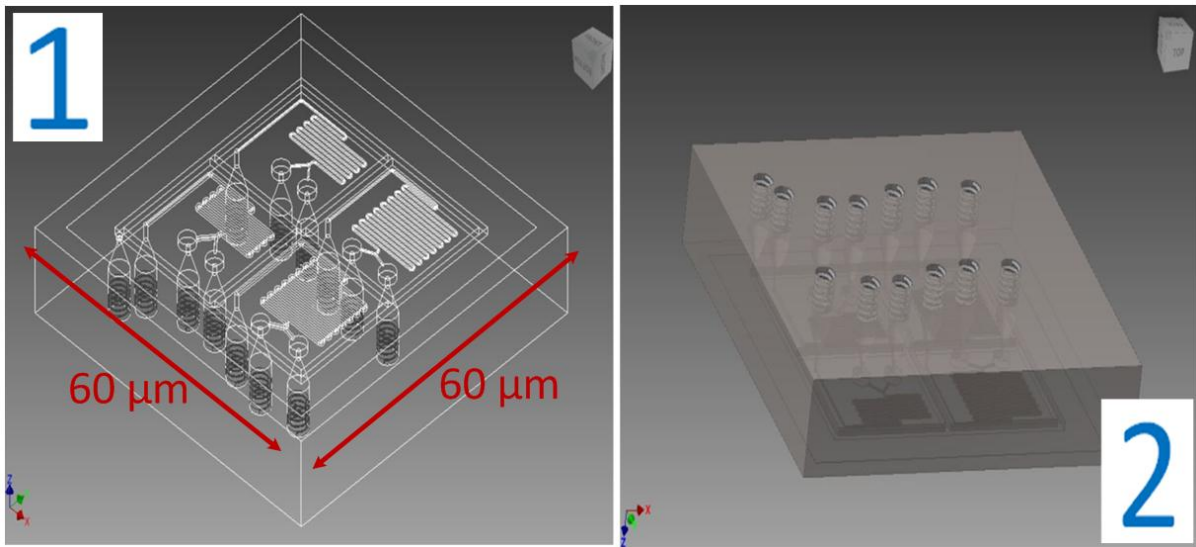


Figure 16: 3D design of the device using Autodesk Inventor, 1) top view, 2) bottom view

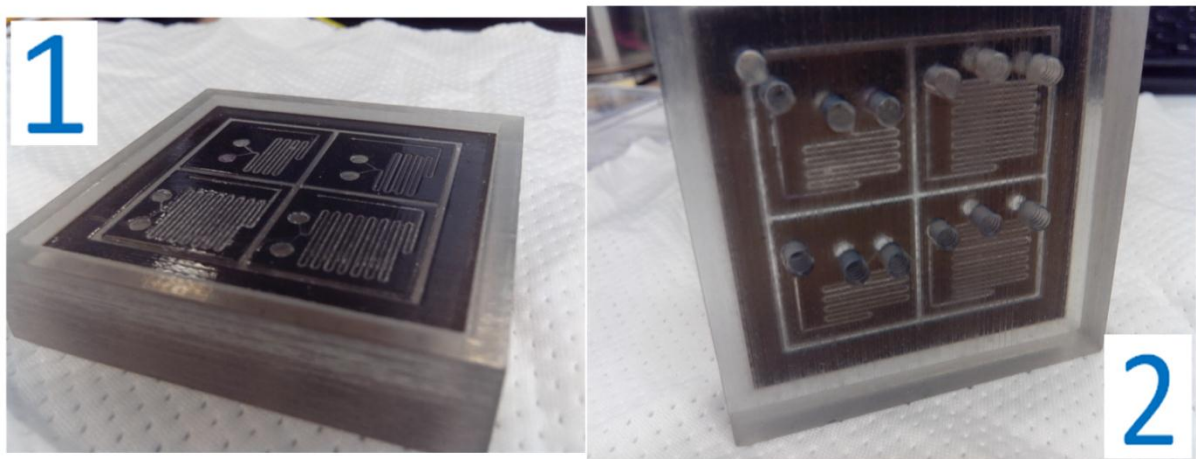


Figure 17: The complete printed channels using 3D printer, 1) top view, 2) bottom view

The device in Figure 17 has different parts:

- a. Black rubber-like part, which is a soft material that acts as a gasket between the glass slide and the device to provide a better seal.
- b. The rest of the device, including the channels, which is a rigid polymer.

- c. The 4 separate sample micro-channels with different depths and lengths to allow a range of flow rates and luminescence intensities to be tested with the same fluids, pumps and cameras.
- d. There are also some wider channels around the sample channels and for holding the glass slide on top of the device using a vacuum pump.

As shown in Figure 17, the main attempt was making as sealed channel as possible. There are other attempts are done to make a perfect sealing for this device such as using Teflon films, Fluorinated Ethylene Propylene (FEP) (A type of polymer with an acceptable flexibility, opposition against chemical reaction and also transparency) etc.

Another challenge associated with printing the device was the removal of support materials, which are printed at the same time as the actual device as a scaffold in the holes and channels to preserve the accuracy of the edges. These support materials are normally removed using a water jet. Unfortunately, this process also destroyed the channels; so removing the support material required a more complicated process:

- a. Remove bulk of support material with soft brushes
- b. Immerse the device in NaOH 7% for about 21 hours
- c. Ultrasonic bath with NaOH 7% for 15 minutes
- d. Wash the device using distilled water
- e. Dry the device using nitrogen

The process may need repeating to completely remove all support material.

The processes of fabricating the channels in this way was more complicated, in terms of cleaning the channels from support material completely and make them empty and required an additional vacuum pump. Despite the extra complexity, the device was not completely sealed and still there were some leakages out of the channels.

In summary, a vacuum-sealed microfluidic device was fabricated by 3D printing but the sealing and device cleaning did not work. It may be possible to produce a printed device with a perfectly flat sealing surface using other types of 3D printers (e.g. one that prints metal). Sealing processes employing other materials (e.g. polytetrafluoroethylene (PTFE)) may also help improve sealing.

## 5.5 Conclusion

As the summary of this chapter, the design, fabrication and sealing of the channel by combining 3D printing and PDMS and oxygen plasma is done and the device is ready to be used in the next chapters.

To reach the final device, some possible ways of fabrication and also sealing processes, which were not as successful as the one mentioned above, were gone through. These steps could be points of interests for future fabrication processes.

## 6 Preliminary validation of flow system and chemiluminescence process

In this chapter the preliminary tests are described. These tests are to confirm that the fluid flow is laminar inside the channels (by measuring the velocity of the fluid inside the channel and also the Reynolds number) and that the chemical mixture chosen for this project produces light. The latter test is done both outside of the channels, in macro size, and inside the channels.

### 6.1 Velocity of micro-beads vs. syringe pump flow rate

The average velocity of the liquid inside the channel depends on the flow rate that is changeable using the syringe pump. To confirm the expected results for the liquid velocity, microspheres of the size of  $5.6\ \mu\text{m}$  are pumped into the channel and single particles tracked by the high speed camera. As shown in Figure 2(a), the microspheres will follow a velocity distribution across the channel.

To start the test, microspheres with a concentration of  $12.5 \times 10^6\ \text{ml}^{-1}$  are diluted in distilled water to a concentration of  $1 \times 10^5\ \text{ml}^{-1}$ . Using a Syringe Pump (Cole-Parmer), the particles were pumped into the channel via a tube of inside diameter of  $150\ \mu\text{m}$ .

There will be some assumption in the calculations to simplify them, such as:

1. Parabolic pattern of the velocity along the fluid flow path
2. The roughness of the inside wall of the channels because of the PDMS roughness
3. Sealing of the PDMS channel by glass at which the pressure for sealing them might change the internal shape and specially the edges of the channel

Calculation of the expected velocity of the particles has been done as follows:

$$\langle V \rangle = \frac{Q}{A} \quad \text{Equation 3}$$

, where  $Q$  represents the flow rate and  $A$  is cross-sectional area.

Figure 18 shows the velocity of the particles for flow rates of  $0.1\ \mu\text{l/s}$  to  $6\ \mu\text{l/s}$ . It is notable that at the lower velocities the spheres wobbled forward and backward in the direction of their velocity because the viscous forces appear at low velocities [33].

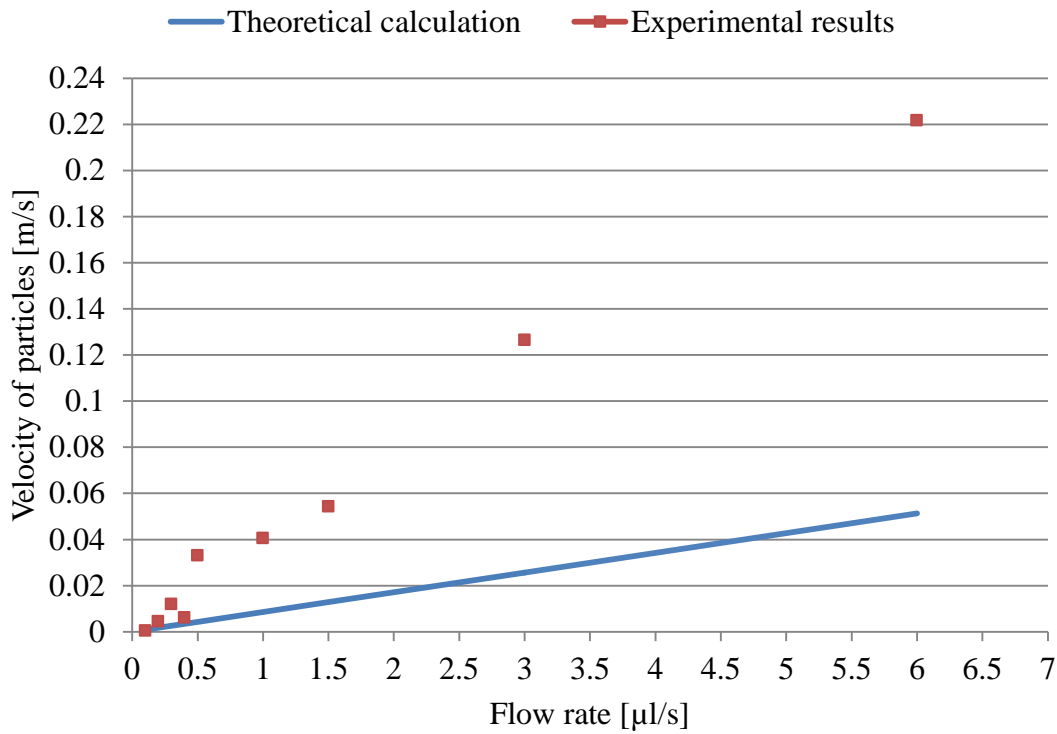


Figure 18: Velocity of the fastest particles passing from the channel centre vs. the calculated average velocity

The theoretical results are calculated from the flow rate of the whole fluid over the cross section of the channel, which is assumed to have rectangular cross section of  $650 \mu\text{m}$  width  $\times$   $180 \mu\text{m}$  depth, are shown by blue line in the figure; on the other hand, red points are the selective fastest particles inside the channel. Looking to these values, the fastest particles are linearly related to flow rate but with a higher slope than the calculated average velocity, as expected. Following calculations are done to quantify this ratio.

Figure 19 shows the velocity of the particles inside a laminar flow follow a parabolic shape (shown in Figure 13) in which the highest velocity is located in the centre and the lowest in the sides.

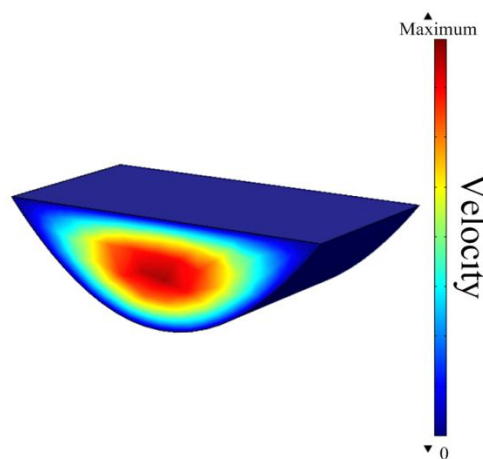


Figure 19: COMSOL simulation results of the velocity of the particles inside the fabricated channel

To compare the fastest particles with the average velocity inside the fabricated channel, first the average point of the parabolic-shape is calculated.

Average point in a parabola is calculated by dividing the surface under the parabola over its width (650  $\mu\text{m}$  in this case).

Equation 4 is the equation of a parabolic shape which is depicted in Figure 20. “a” is the constant that is calculated using the actual values of the fabricated channel, which are shown in Figure 20.

$$Y^2 = 4ax \quad \text{Equation 4}$$

On the other hand, Equation 5 calculates the half area under the parabola as shown shaded in Figure 20;

$$\int_0^D \left( \frac{Y^2}{4a} - C \right) dy = \text{half area} \quad \text{Equation 5}$$

where D is the depth (180  $\mu\text{m}$  in this case) and c is a constant (180  $\mu\text{m}$  in Figure 20); and the whole area is the calculated area multiplied by 2.

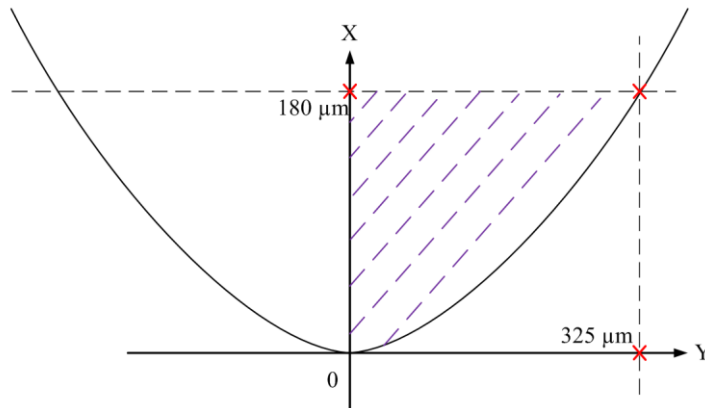


Figure 20: Parabolic cross-section of the channel

Putting values and doing the calculations, the area under the parabola cross-section of the channel will be  $\approx 39040 \mu\text{m}^2$ . By dividing this value by the cross-section width, the position of the average velocity of the particles is calculated ( $\approx 60 \mu\text{m}$ ). The average points are shown in blue in Figure 21. So the fastest particles velocities that are traveling in the central line of the parabolic cross-section are about 33.3% above the average velocity. Calculating the ratio of the fastest selected particles over the average velocity of the particles from Figure 18 is about 28% ( $(V_{\text{exp}}/V_{\text{theor}}) > 2$ ). The reason for the difference is that the ratio of 33.3% is calculated theoretically by taking the actual fastest particles' places crossing from the central line of the parabola whereas the ratio of 28% is calculated by taking to account the fastest velocity of the experimentally found particles which are not necessarily those which are crossing exactly from the centre and this is confirmed by checking the places of the experimented particles along the channel. So by a good approximation, the measurement and the experimental results match.



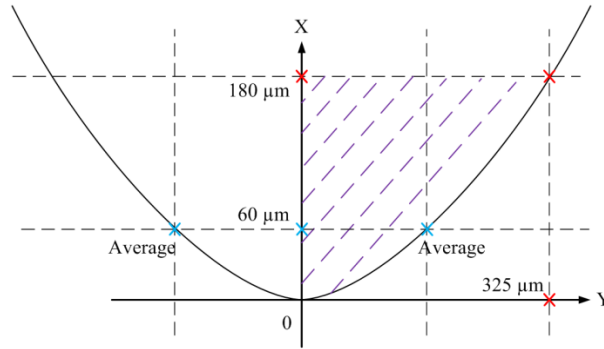


Figure 21: Average points of the parabolic cross-section of the channel

Having found about the velocity the Reynolds number is calculated using Equation 6:

$$Re = \frac{\rho < V > L}{\mu} \quad \text{Equation 6}$$

where  $\rho$  is the viscosity,  $< V >$  is the average velocity of the particle calculated above,  $L$  is the length of that the liquid pass along the channel and  $\mu$  is the dynamic viscosity.

Figure 22 shows the calculated Reynolds number as a function of flow rate. These data demonstrated that even in the flow rate of 6  $\mu\text{l/s}$ , the flow will be laminar and that with a further increase in the flow rate, the fluid is behaving in transitional flow as the Reynolds number exceeds 2100.

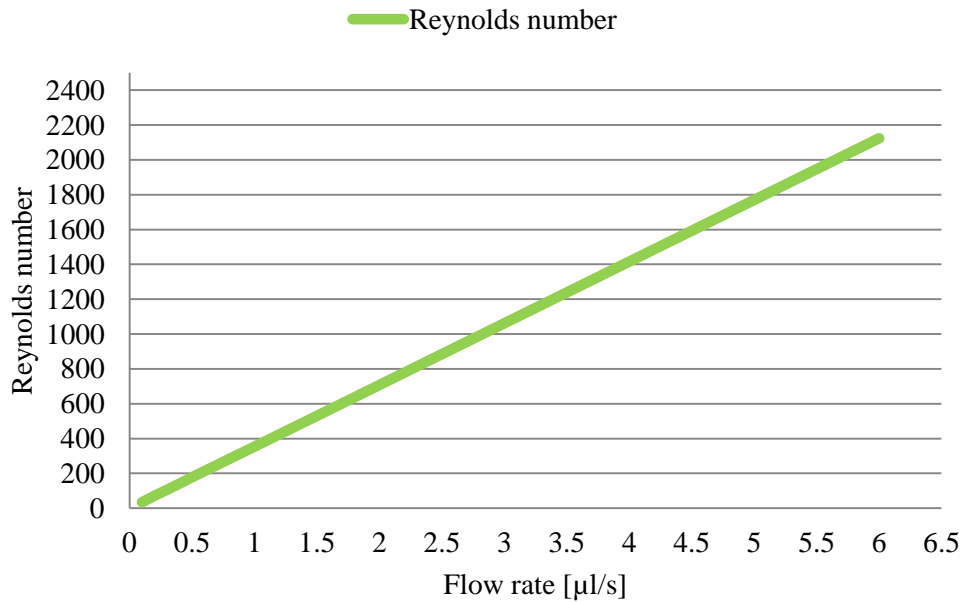


Figure 22: Reynolds number vs. flow rate

In conclusion, the velocity of the particles validated by comparing them with the theoretical calculations. The Reynolds number is checked to confirm the laminar behaviour of the liquid inside the channel.

## 6.2 Preparing and mixing chemicals:

Before starting the microfluidic experiment and finding the results, target chemicals were tested to confirm that their reaction produces light. To do this, two sets of tests were carried out: mixing chemicals outside of the channels and mixing them inside channels

The experiment is carried out in 5 steps:

- 1) Mix two chemical fluids in order to prove the light emission as result.
- 2) Repeat the previous step inside the chip.
- 3) Prepare fluids with different concentrations and repeating step 2.
- 4) Analyse and processing the resulting image using MATLAB software.
- 5) Measure the minimum detectability of the CCD camera available in the lab.

The two mixtures are used in this experiment are as follows:

Luminol (0.4g), sodium hydroxide (4.0 g), sodium hypochlorite (50 ml), water (1950 ml);

Two fluidic chemicals which are used in the experiment are as follows:

Bottle “A”: water (1000 ml) + NaOH (4.0g) + luminol (0.4 g)

Bottle “B”: water (950 ml) + NaOCL (50 ml)

The reaction of these chemicals is shown in Figure 23 where red circles showing the bonds brake to produce the required energy for exciting electrons.

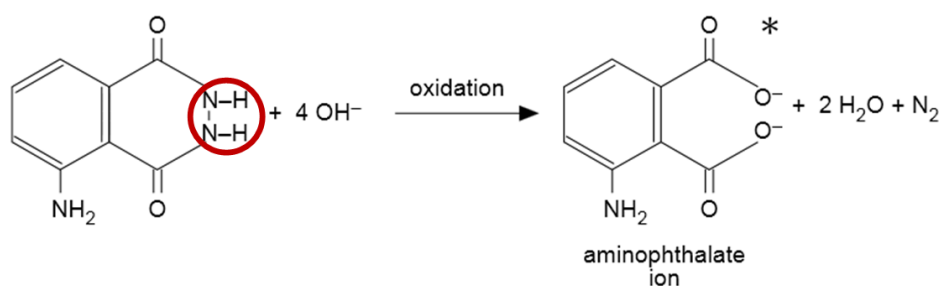


Figure 23: Chemical reaction between the materials to create the required energy for exciting electrons [34]

Mixing the chemicals of bottle A and B in a separate bottle and putting the bottle beside a spectrometer, an emission spectra with two peaks with 452 nm and 489 nm will be measured and these two peaks are basically related to the bonded and not bonded aminophthalate ions (shown in Figure 23) in the reaction [35][36].

Mixing the chemicals is tested inside the channels and the resultant light, which is grabbed by the camera, is shown on Figure 24.



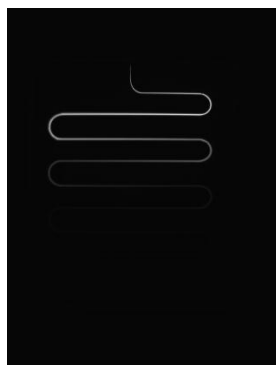


Figure 24: The resultant light after mixing in the channels

### 6.3 Flow rate dependence:

In this section the chemicals are mixed in different luminol concentration from 0.4 g to 0.004 g in 100 ml of 'NaOH + water' solution and flow rates from 0.1  $\mu\text{l/s}$  to 4  $\mu\text{l/s}$ . There are two reservoirs designed in the device which the fluids of bottle A and bottle B are pumped through them into the channel. Since the goal of experiment is to get information about the effect of the flow rate and luminol concentration on the intensity of the light, the test is done in several steps in which the concentration of the luminol in the sodium hydroxide and water is changing.

The amount of the chemical that is used in this section is the same for bottle B and bottle A. Luminescence power along the length of the channels gives information on mixing and lifetime of chemiluminescence (examples of the different power values changed by different parameters are shown in Figure 25 and Figure 26).

Sodium hydroxide and water are mixed with the same ratio mentioned. The first step is pumping the fluid in different flow rates to be mixed with the fluid of the second reservoir (bottle B) that is going to be pumped with a fixed flow rate of 0.5  $\mu\text{l/min}$ . Figure 25 shows an example of the light in two different luminol concentrations.

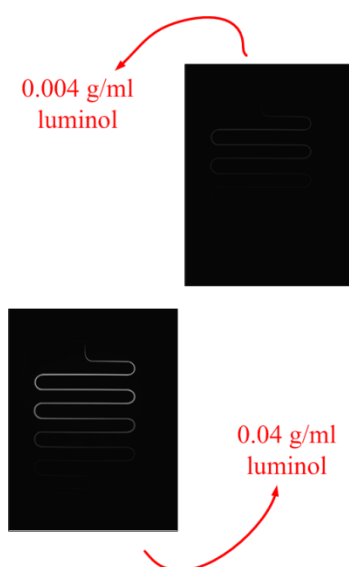


Figure 25: An example of chemiluminescence light in the flow rate of 0.3  $\mu\text{l/s}$  in the microchannels

Figure 26 shows the effect of increasing the flow rate by increasing the flow rate of the fluid containing the luminol.

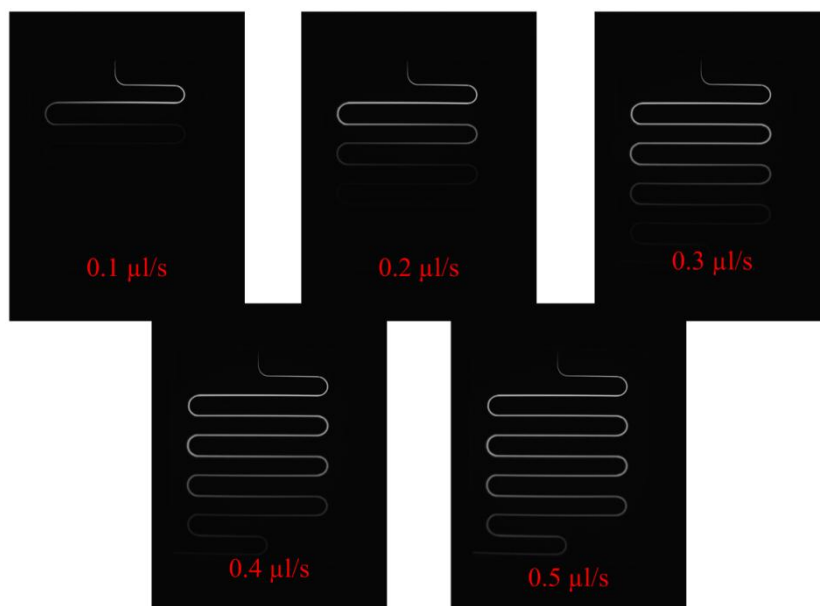


Figure 26: The effect of increasing the flow rate of the solution containing luminol of the concentration of 0.04 g per 100  $\mu$ l of the solution of NaOH and DI Water

As a conclusion, mixing of chemicals is tested in this section out of the channel and also inside the channel. The results show an increase in the luminescence light power by increasing the luminol concentration and an expansion in the luminescence intensity by increasing the flow rate.

## 6.4 Conclusion

As a conclusion, in this chapter the primary tests are accomplished to check the validity of velocity calculation regarding the average velocity of the liquid in the channel. Using the confirmed values, Reynolds number inside the channel checked regarding the validity and the 6  $\mu$ l/s is chosen as the threshold for the transitional flow. Selected reaction chemicals are tested to check whether their reaction produces light or not and this test performed outside and inside of the channels.

## 7 Image and data analysis

Two methods used to analyse the images are described in this section. These methods are briefly:

1. Integrating values of all pixels within a predefined box over the image (shown by red box in Figure 28). The box covers whole length of channel excluding some reflected light in the images. Value of each pixel represents the intensity of light at a specific point on the device observed by camera. Therefore the result of this integration determines the total emitted light by the device which varies with different flow rates and concentrations of luminol.
2. Fitting a pattern over the design to allow determination of emitted power vs. length to illustrate the effect of the flow rate and also the luminol concentration on the power vs. position along the channel.

To ensure robustness and reliability, measurements have been repeated 15 times for each concentration and flow rate. This is depicted in below diagram (shown in Figure 27);

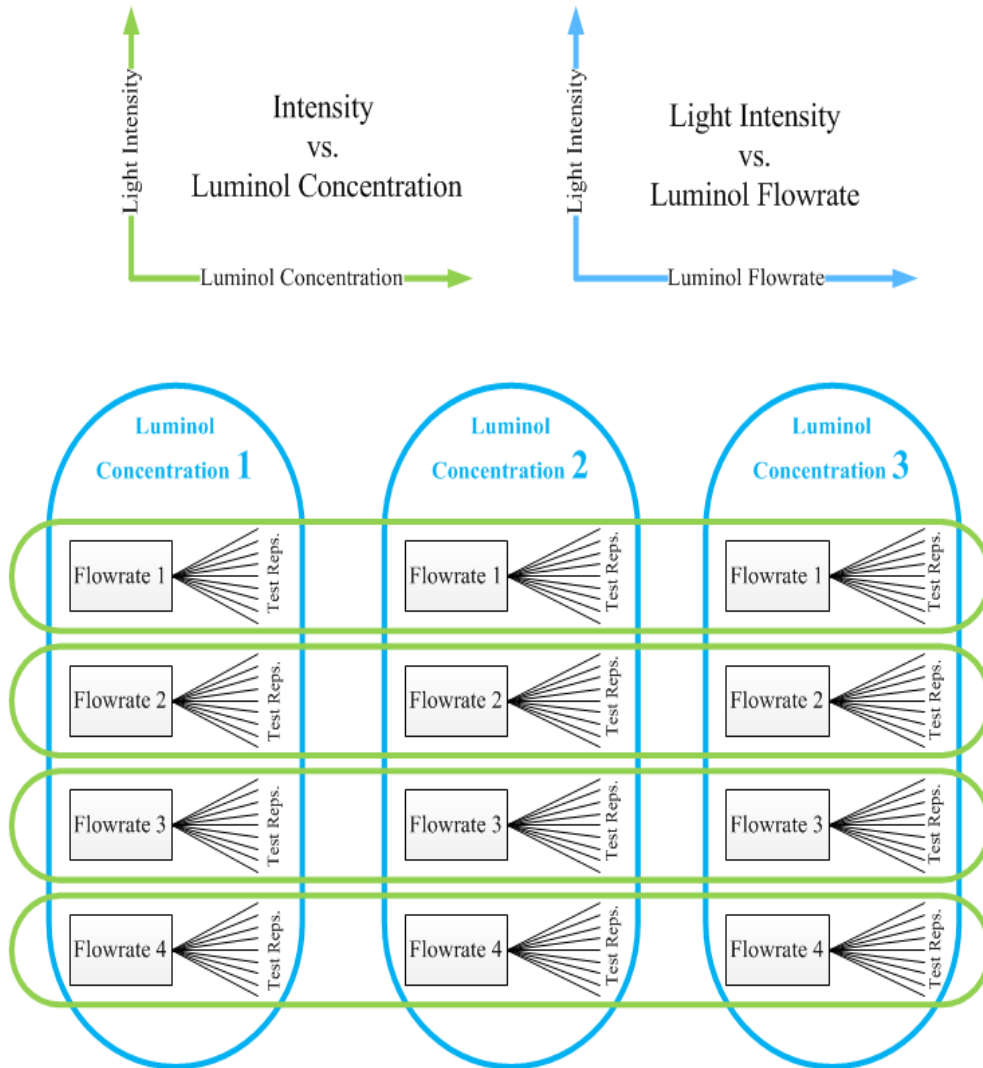


Figure 27: The images arrangements used for analysing them

## 7.1 Method 1

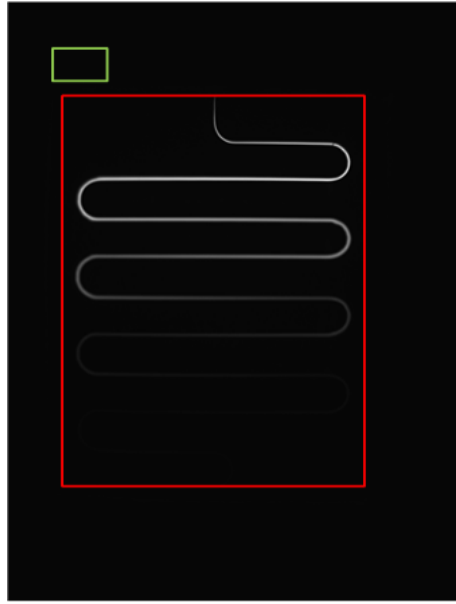


Figure 28: A box covering the setup

Figure 29 shows a flowchart representing method 1 for calculating the effect of luminol concentration and flow rate changes on the total intensity of the light. The steps of this algorithm are as follows:

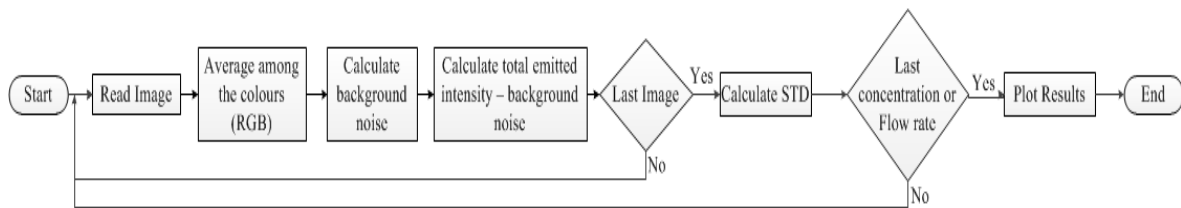


Figure 29: Flowchart of the first method for each concentration and flow rate

1. Reading a colour image and calculating the average of red, green and blue  $\left(\frac{R+G+B}{3}\right)$  values of each pixel.
2. Using the green box in Figure 28 to calculate the background noise of the image.
3. Using the red box and calculating the emitted light's average intensity inside it.
4. Subtracting the background noise from the calculated intensity.
5. Repeating above for all images captured for a specific flow rate and luminol concentration and calculating the STD and error bars for the results.
6. Repeating above for all flow rates and luminol concentrations and comparing the results.

### 7.1.1 Results for method 1:

The analysis of the images using this method and also their discussion are done in this part. To find the limit of detection, the experiment has been repeated for 5 concentrations in addition to the water. Also, a series of 10 flow rates were tested in order to investigate the effect of flow rate on the intensity of the light.

The limit of detection, which is going to be measured in this section, is described by a chosen factor of the standard deviation, which depends on the certainty of confidence required. The standard deviation represents the uncertainty of the measurement taken from a sample within a population [37].

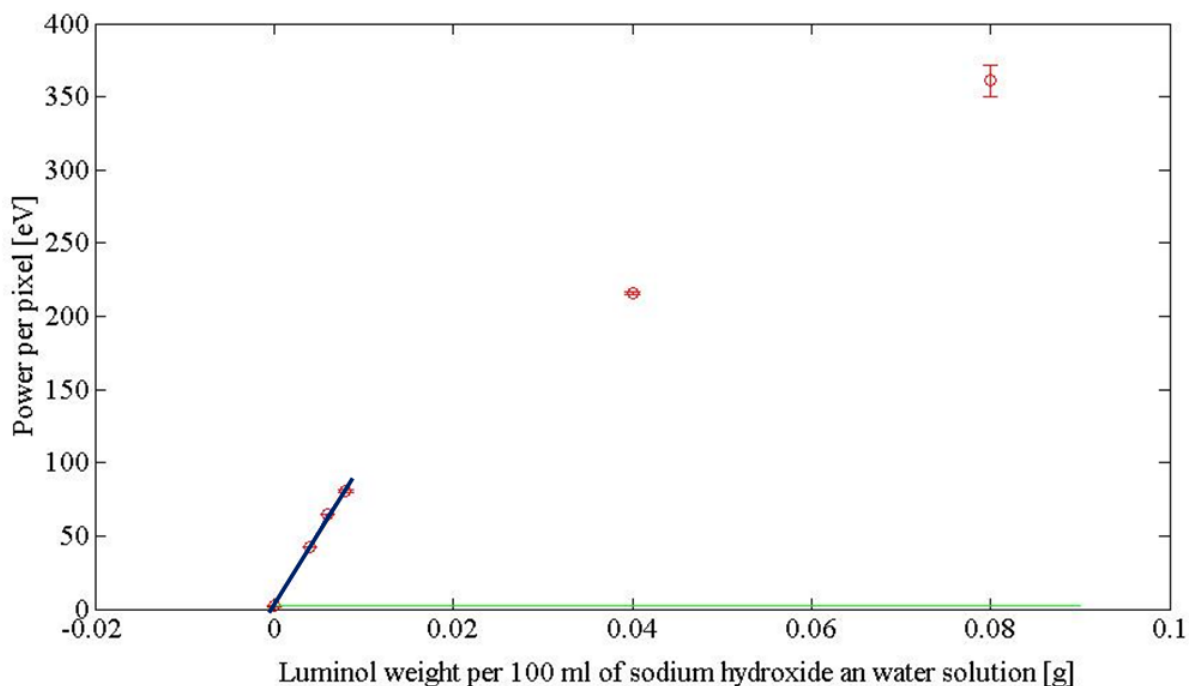


Figure 30: The intensity of light in different concentrations

Figure 30 is showing the intensity of the light in one flow rate ( $0.75 \mu\text{l/s}$ ) and different concentrations of luminol. It is notable that the noise is filtered from the whole image that means the zero level is noise level. The red bars are the error bars defined by the 3 standard deviation, from the American statistical association defined value, and the green line represents the 3 standard deviations above the zero level and will be used in limit of detection determination.

There was two limits which the experiment couldn't be repeated for more concentrations, one in higher concentrations e.g. 0.4 g of luminol in which the reaction between luminol and PDMS creates bubble that stuck in the channels. In this case the analytical results are not reliable. The other limit is at the low concentration such as 0.004 g of luminol because of the high exposure time requires for detecting the intensity of the light in the channel; increasing the exposure time to more than 10 seconds causes the surrounded areas to be seen on the other hand, the amount of extra noise along the whole image increases which again decrease the accuracy of analysed data and also their reliability. As an example the data point of zero concentration that is literally just water passing pumped in the channels, is showing some intensity value event with no chemiluminescence light. The main reason is the high exposure time that increases the noise especially in the edges, which its effect comes to the picture while analysing the images when the whole image pixel values are averaged.

The points in Figure 30 are showing that for higher concentrations of luminol the intensity begins to approach a saturation point while for lower concentrations of luminol the intensity as a function of concentration follows a linear relationship as is observed in the literature [38].

In Figure 30, 3 standard deviations above the noise level (zero line in this figure that is shown by the green line), the limit of detection is determined in a value lower than  $4 \times 10^{-6}$  g of luminol concentration.

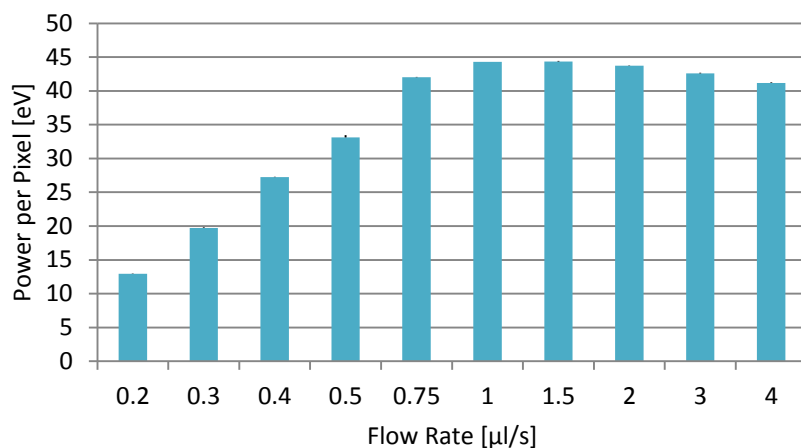


Figure 31: The effect of the flow rate on total intensity of the light

Next figure (Figure 31), shows the effect of the flow rates on the intensity of the total light. As the figure showing, intensity is increasing by moving to the higher flow rates and then it reaches to its peak at  $1 \mu\text{l/s}$  to  $1.5 \mu\text{l/s}$  where it starts to decrease and this saturation is because of the small size of the channels. In higher flow rates, the reaction happens in a further distance where it requires longer channel to be able to mix the chemicals and produce the light.

As a summary, using this method the limit of detection for luminol is determined lower than  $4 \times 10^{-6}$  g in 100 ml of the solution ( $< 40$  ng/ml). The effect of the flow rate on the intensity of the light is also shown in Figure 31 where the total intensity is increased by increasing the flow rates and also discussed that to measure the total intensity of the light in the higher flow rates, longer channel required.

## 7.2 Method 2

In this method, the emitted intensity is integrated across the channel (along the white dash line in Figure 32) and the resultant power is calculated in different positions along the length of channel.

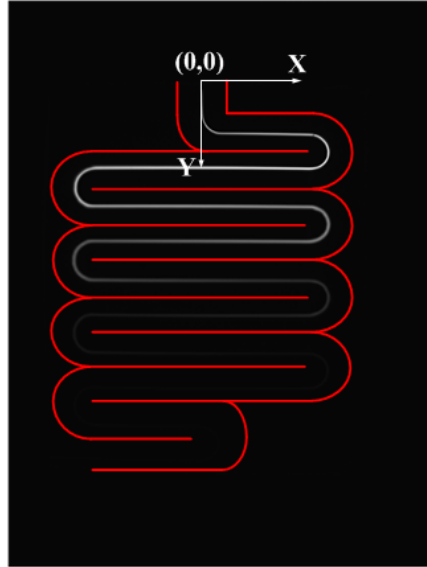


Figure 32: A predefined pattern covering the channel

A pattern (red line in Figure 32) is drawn over the image. This pattern is obtained based on the values used for the layout. Analysing images using this method requires more calculation and that is because of using a lens on the camera which changes the pixel size and resolution of images. This process is calculating the intensity of the light between chosen points on the pattern by drawing lines between them and calculating the intensity (shown in Figure 33).

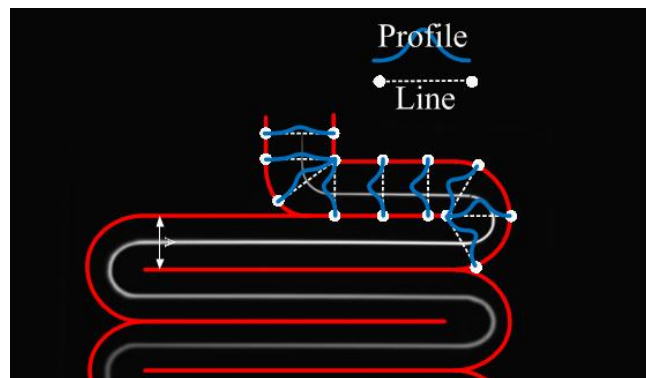


Figure 33: The demonstration of the idea at the back of having a pattern over the channel

Although a careful alignment has been considered to locate the device flat and position the channels horizontal, due to lens effect and holders' instability, an image with slightly tilted channels may obtain from time to time. A part of algorithm in second method is correcting for this tilt effect which is explained in the following.

In short, the algorithm does as in Figure 34:

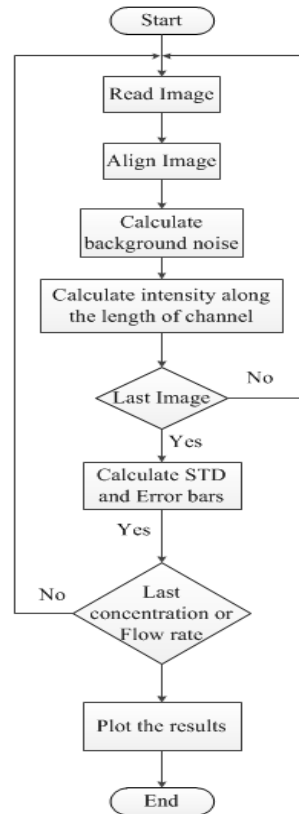


Figure 34: The flowchart for the code which has used the red pattern over the channel

Each box in the above chart is explained in the following:

**i. Reading:**

Reading an image as well as calculating the average of red, green and blue values of each pixel.

**ii. Background noise calculation:**

Using the green box to calculate the background noise of the image.

**iii. Alignment:**

Angular misalignment of images collected during time to time has been corrected by introducing channels middle lines. To find the middle lines, first of all, two parallel lines are drawn where they cross the channels (shown in Figure 35). Second, the best fit to the intensity profile along these lines are found. Third, the maximum intensity points along the profile are calculated and their middle points are found (shown in Figure 36). Forth, using two of the middle points, the middle line is drawn (shown in Figure 37). Fifth, the slope of this line is calculated and finally the image is rotated with this angle.



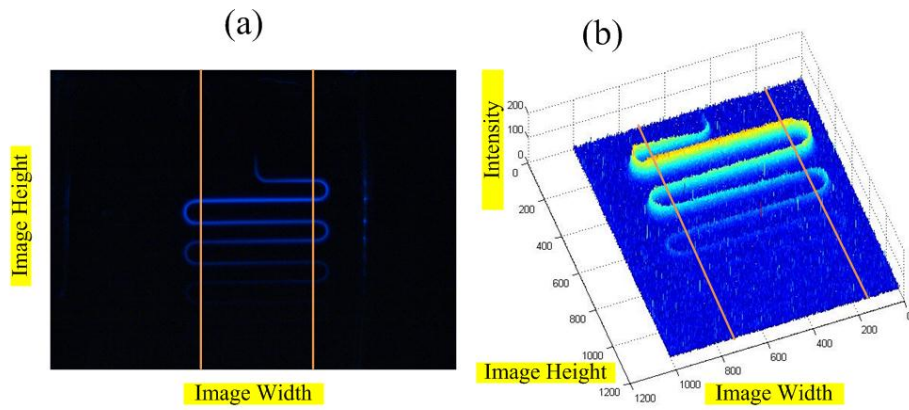


Figure 35: An image by the lines introduced to get the maximum points of the intensity, a) 2D view of the image, b) 3D view of the image (MATLAB)

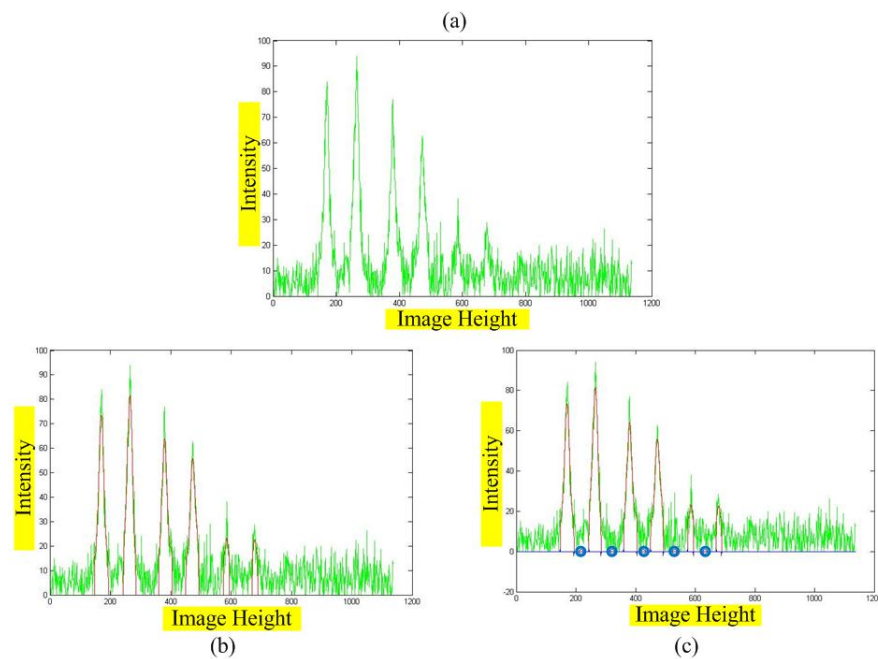


Figure 36: a) intensity along one of the lines, b) finding the best fit for the intensity and removing the noises, c) finding the maximums and alternatively middle points which has been illustrated by blue circles (MATLAB)

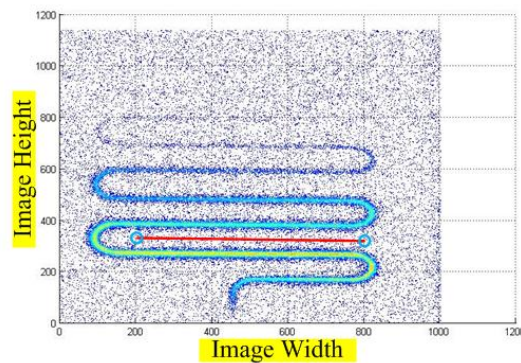


Figure 37: Using two blues circle points and draw the red line between them (MATLAB)

This misalignment is because of the 3 reasons:

- Sample was not secured properly
- CCD was not secured properly
- The CCD was not aligned properly

These issues were checked in the final experiment.

**iv. Intensity calculation:**

Intensity calculation using this method is possible when the pattern (the red one in Figure 32) is fitted in the right place over each image. In other words, there is an origin required for the image to be fitted with the pattern's origin (shown in Figure 38 and Figure 39).

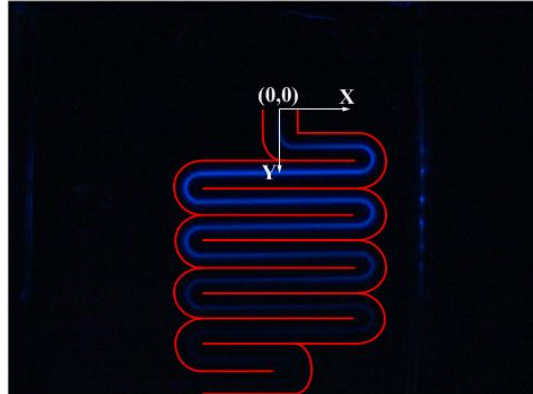


Figure 38: Demonstration of the introduction of an origin for each image

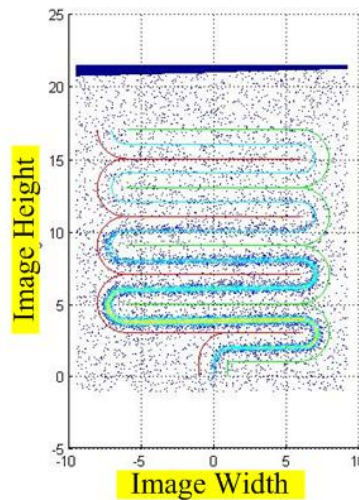


Figure 39: Pattern on top of the image

Using the camera's technical detail and doing the following calculation, the intensity of the light is converted to power.

It starts from the quantum efficiency of the camera which shows the number of photons which is converted to electrons in its sensor. There is also another value which shows the maximum electron capacity of the sensor in its high dynamic mode. By putting the camera in its high dynamic mode and also taking images in 16 bit mode, we are able to use this number which is 36000 and using the equation below, the equivalent value of energy for each pixel in which that pixel will have the highest intensity of  $2^{16} - 1$ , is calculated.

$$E = nh\theta \quad \text{Equation 7}$$

, in which  $n$  is the number of photons,  $h$  is Planck Constant and  $\theta$  is the frequency of the light. The wavelength of the light in this experiment is  $\lambda = 489 \text{ nm}$ .

And finally the power would be calculated using the equation bellow:

$$P = \frac{W}{T} \quad \text{Equation 8}$$

, where  $W$  is the amount of the Energy and  $T$  is the Exposure time which is being chosen for each test.

Since the intensity of the light in this method is calculated along 2 mm across the channel, the unit of the power is going to be per meter. In other words the unit will be the power density over a line of 2 mm [eV/m].

These calculations should be affected on all the images using two “FOR” loops; one for repeating the process over those 15 repeated images of the same flow rate in one concentration and another one for repeating that for other concentrations.

Totally, accepting the complexity of the code and spending more time on writing it to align images, find the actual pixel size, put the predefined mask over the image etc., would be valuable and give more detailed results.

### 7.2.1 Results for method 2:

The explanation and also the results of the images using this method are done as follow;

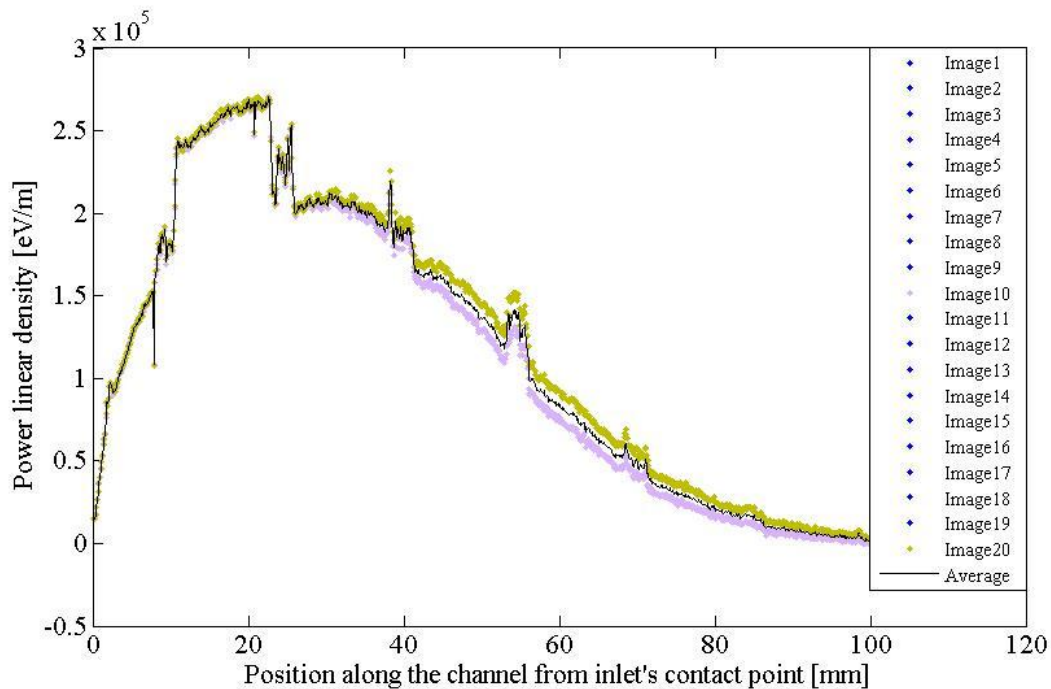


Figure 40: Average figure plotted having 20 separate figures for the concentration of 0.008 g luminol in the flow rate of 0.3  $\mu\text{L/s}$

The first figure in this part (shown in Figure 40) is basically showing the process of plotting an average figure (black line in Figure 40) of 20 figures. Peaks in this figures illustrating the

high intensity of the light in the corresponding distances from the beginning of the mixing area. These peaks are corresponding to bends where the liquid velocity is more than those in the straight part of the channel.

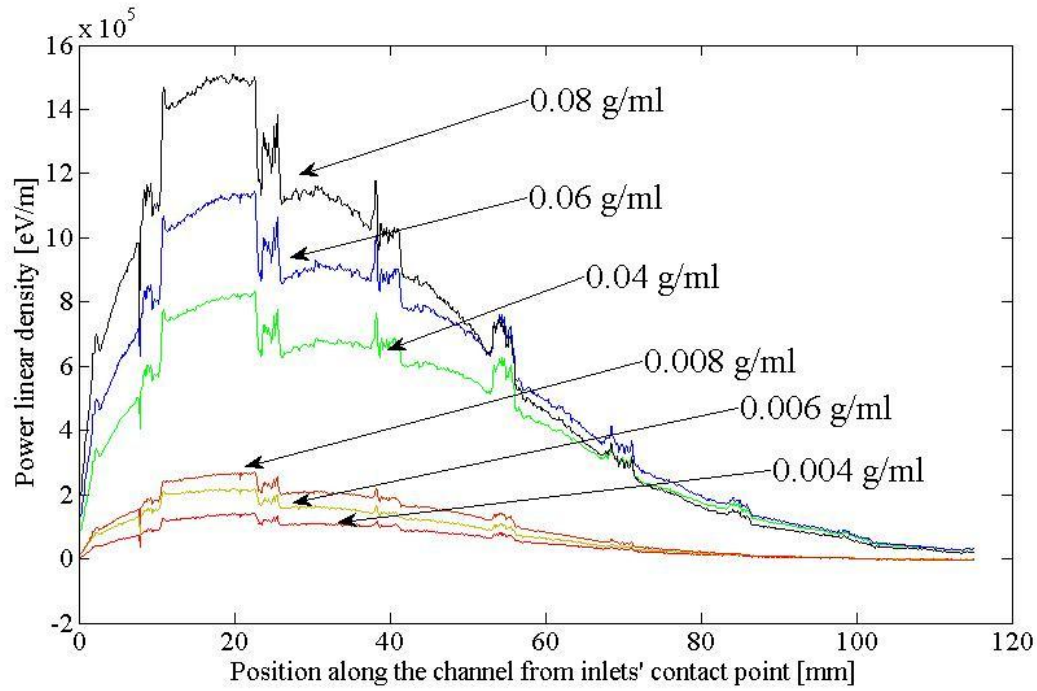


Figure 41: The intensity of the light in different concentration of luminol

Figure 41 shows the increase in the power of the intensity of the light by increasing the concentration. It also shows that peaks and by checking the position of these peaks they turned out as bends which shows that there are more mixing and more light intensity as the result of the dean flow in the bends along the channel.

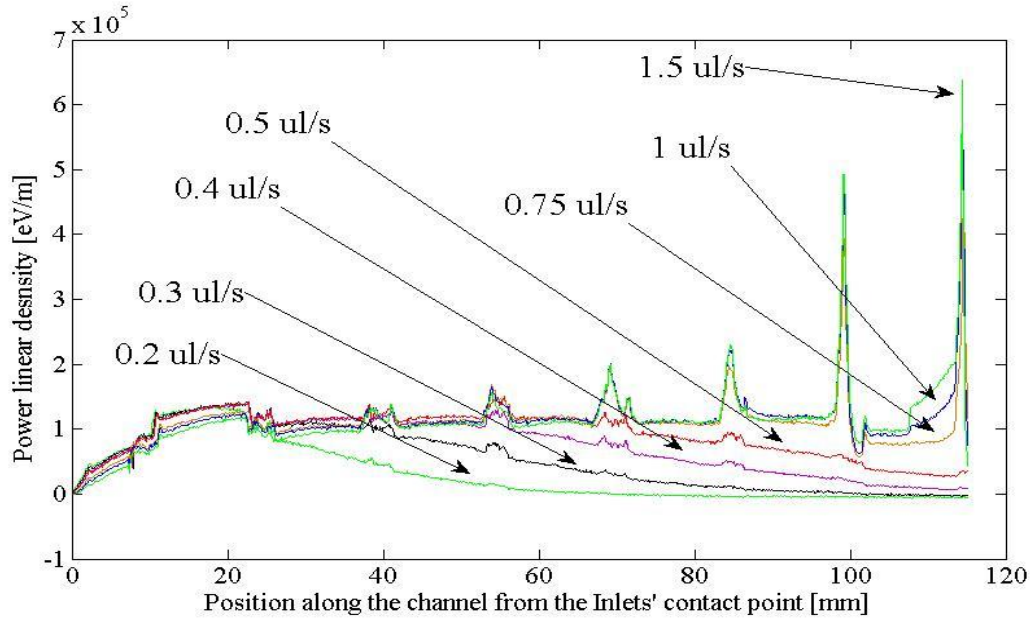


Figure 42: Flow rate effect on the intensity of the light along the channel

Figure 42 shows the effect of increasing the flow rate on the power of the light in the channel; there are basically three things happen in the figure: 1. the intensity of each points increases because of having more chemicals reacting in a same time, 2. the intensity increases along the channel which literally demonstrates the light expansion along the channel and that is because of having more mixing along the channel since the chemicals are pushing faster; also the intensity at the beginning of the channel decreases , 3. the intensity of the light in the bends increases and that is because of having more chemical reaction since more chemicals are pushing through and also high velocity of particles which produce even more velocity in bends.

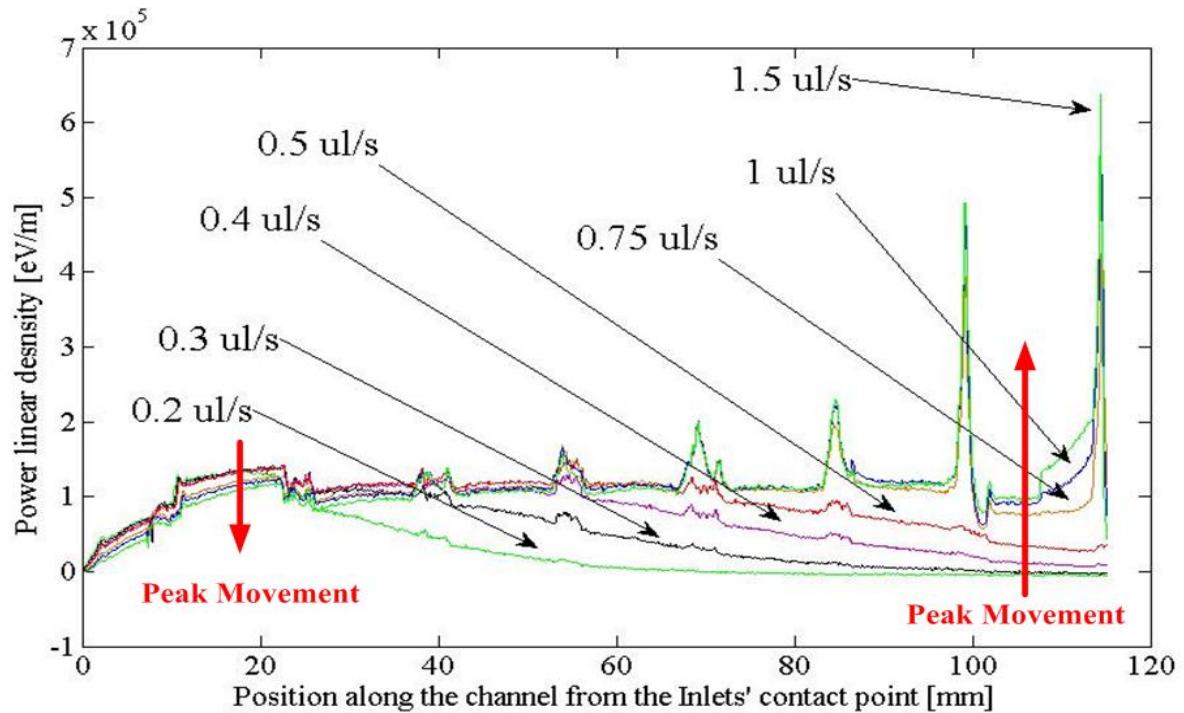


Figure 43: Movement of the peaks by increasing the flow rate

Figure 43 is actually the data shown in Figure 42 with green arrows. In Figure 43, decreasing the light intensity at the beginning point and also increasing of the peak at the final end all is shown using those green arrows. Higher flow rates, alternatively result in the expansion of the light inside the channel which shows that more chemicals have chances to collaborate in the reaction and creating the light. In other words, as Figure 18 shows, in a low flow rate such as  $0.3 \mu\text{l/s}$ , the velocity of the particles is about  $0.01 \text{ m/s}$ ; using this value and calculating the time period which takes for the fluid particles reach to the length of  $120 \text{ mm}$ , is  $12 \text{ s}$ ; whereas this number for the same fluid in the flow rates of  $4 \mu\text{l/s}$  which the velocity of particles in that is about  $0.12 \text{ m/s}$ , is  $1 \text{ s}$ . This calculation shows that the time which the volume of the liquid requires to reach to the  $120 \text{ mm}$  length in low flow rate is about  $\times 12$  more than its value in high flow rate. Then the reaction has been terminated in low flow rate case before they reach to that point and equivalently there won't be much light left whereas in high flow rate they mix mostly at the end.



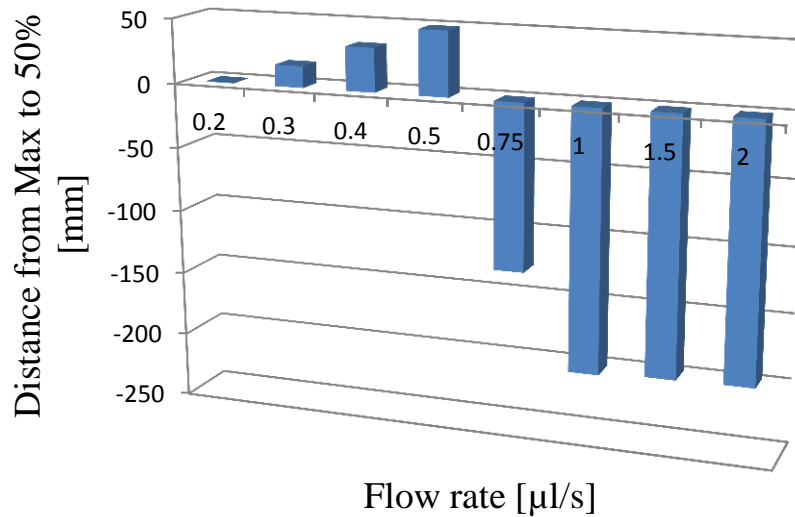


Figure 44: Distance from the maximum of the light intensity peak

It's notable that, although using the optical breadboard, attempting to not touch the setup during the experiment and so forth could decrease the external effects on images, but sometimes, human errors like the eye errors in aligning the channel could not be negligible on taken images. Aligning these images would be another issue which might make the calculation of even more complex.

One of the main aims for method 2 was looking at the light decay length changes from its maximum intensity in different flow rates. Figure 44 shows the distances in which the peak of the light intensity in its maximum value reaches reach its 50% value. Figure shows that the intensity (Power) drops faster when it's in low flow rate and it is true between  $0.2 \mu\text{l/s}$  to  $0.5 \mu\text{l/s}$  and after that because of the expansion of the intensity, the level of the light intensity reaches to +50% which could be in infinity in this case.

## 8 Nanoparticle enhancement of chemiluminescence

### 8.1 Introduction

Chemiluminescence technology has a weak resultant light. So it requires an improvement for its detection limit to improve the bioassay-sensitivity [39].

The aim of this chapter is to demonstrate the effect of employing nanoparticles to increase the intensity of the luminescence light. Based on the literature review [39][40][41], surface plasmon is the first principle that is been shown regarding the nanoparticles and enhancement of the chemiluminescence using them. So one of the sections in the whole chapter is to give a brief introduction of the surface plasmon as well as chemiluminescence lifetime of the event and evanescent field calculation. Following these summaries, the additional steps are given to conduct this experiment are briefly explained.

Surface plasmon (SP) is a free electron oscillation on the surface of the metal-dielectric contact surface [42]. Visible light is an electromagnetic wave, which is electric and magnetic fields propagating towards the direction of the light motion while they are perpendicular each other and the direction. Visible light follows the same rule in terms of containing electric and magnetic field with its electric field oscillation rate of about  $10^{15}$  cycles per second [43], which pushes the free electrons of metal oscillate close to the surface of the material.

Enhanced chemiluminescence is been a subject of the study in the recent years as in in 2006, Chowdhury et al. [44] used silver island film and enhanced the luminescence intensity by the factor of 20. Using the silver film, Aslan et al. enhanced the chemiluminescence light by the factor of 5 [39]. In 2009, Chowdhury et al. gave a review on the works have been done regarding the enhancement of chemiluminescence using metal-enhanced chemiluminescence and microwave-triggered metal-enhanced chemiluminescence [45].

Oscillations of the free electrons in silver and gold nanoparticles happen under specific conditions which correspond to the material properties and also the special frequencies. Two of these materials, which are the target of the study, are gold and silver.

In this chapter, a brief introduction of the surface plasmon is given; with two key factors, metal properties and frequencies, the plasmon on the surface are described.

### 8.2 Evanescent field calculation

The purpose of the calculation is to find out what proportion of the liquid is exposed to the nanoparticle evanescent field, hence what enhancement might be observed.

In order to determine this, an assumption, in which just 10 nm distances far from the surface of the nanoparticles would be in the evanescent field, is made following reference 46. First, the volume of the sphere surrounding the particle with a diameter of (nanoparticle diameter + 20 nm) needs to be calculated and then subtract this diameter from the volume of nanoparticles.

$$\frac{4}{3} \pi \left[ \left( \frac{D_{\text{NPs diameter}} + 20 \text{ nm}}{2} \right)^3 - \left( \frac{D_{\text{NPs diameter}}}{2} \right)^3 \right] \quad \text{Equation 9}$$

This calculation gives the volume of the liquid which would be affected by each nanoparticle, being illustrated in Table 3 for different diameter.

Nanoparticles type	Silver and Gold		
Nanoparticle diameter	20 nm	40 nm	60 nm
The volume of additional 10 nm diameter which has surrounded nanoparticles	$\sim 29.4 \times 10^{-24} \text{ m}^3$	$\sim 79.8 \times 10^{-24} \text{ m}^3$	$\sim 155.4 \times 10^{-24} \text{ m}^3$

Table 3: The volume of liquid effected in 10nm distance from the surface of spherical nanoparticles

Having these numbers, the total volume which is being affected in each case by multiplying them into the number of particles in 1 millilitre. Table 4 is showing the number of particles in ml after diluting it inside the solution of luminol.

NPs Type	Silver			Gold		
Nanoparticle diameter	20 nm	40 nm	60 nm	20 nm	40 nm	60 nm
Starting particle concentration (SC) (SC) $\left( \frac{\text{Particles}}{\text{m}^3} \right)$	$\sim 7 \times 10^{16}$	$\sim 9 \times 10^{15}$	$\sim 2.6 \times 10^{15}$	$\sim 7 \times 10^{17}$	$\sim 9 \times 10^{16}$	$\sim 2.6 \times 10^{16}$
Diluted value (DV) $\left( \frac{\text{Particles}}{\text{m}^3} \right)$	$\sim 3.5 \times 10^{16}$	$\sim 4.5 \times 10^{15}$	$\sim 1.3 \times 10^{15}$	$\sim 3.5 \times 10^{17}$	$\sim 4.5 \times 10^{16}$	$\sim 1.3 \times 10^{16}$

Table 4: The number of particles in  $\text{m}^3$

Having the number of diluted particles for each size and type, the average distance between two particles, by doing the calculation like as it has been shown as follows, could be determined (shown in Table 5);

Assuming that each particle is sitting in the middle of the cube, the dimensional analysis of this calculation is shown below.

$$\left( \frac{\text{Particles}}{\text{m}^3} \times \frac{1}{\text{Particles}} \right) \rightarrow \sqrt[3]{\frac{1}{\left( \frac{1}{\text{m}^3} \right)}}$$

The reason for checking the distance between nanoparticles is to find (on average) how big the cube of liquid is that surrounds each sphere.



Figure 45 is showing the idea of the calculation made above;

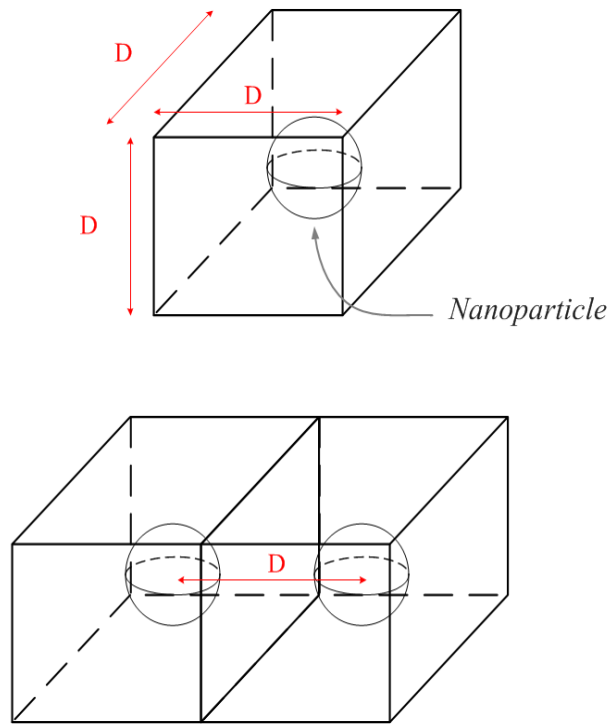


Figure 45: Picture related to Table 4

NPs Type	Silver			Gold		
Nanoparticle Sizes	20 nm	40 nm	60 nm	20 nm	40 nm	60 nm
(DV) ( $\frac{\text{Particles}}{\text{m}^3}$ )	$\sim 3.5 \times 10^{16}$	$\sim 4.5 \times 10^{15}$	$\sim 1.3 \times 10^{15}$	$\sim 3.5 \times 10^{17}$	$\sim 4.5 \times 10^{16}$	$\sim 1.3 \times 10^{16}$
Average distance between each two particles (D) (m)	$\sim 30.6 \times 10^{-7}$ $\approx 3060 \text{ nm}$	$\sim 60.6 \times 10^{-7}$ $\approx 6060 \text{ nm}$	$\sim 91.6 \times 10^{-7}$ $\approx 9160 \text{ nm}$	$\sim 14.2 \times 10^{-7}$ $\approx 1420 \text{ nm}$	$\sim 28.1 \times 10^{-7}$ $\approx 2810 \text{ nm}$	$\sim 42.5 \times 10^{-7}$ $\approx 4250 \text{ nm}$
Volume of the cube with sides of D ( $\text{m}^3$ )	$\sim 2.86 \times 10^{-17}$	$\sim 2.22 \times 10^{-16}$	$\sim 7.68 \times 10^{-16}$	$\sim 2.86 \times 10^{-18}$	$\sim 2.21 \times 10^{-17}$	$\sim 7.67 \times 10^{-17}$

Table 5: Results of diluted value from Table 4, average distance of each two particles and volume of the cube from Figure 45

The final step is determining the percentage of the nanoparticles and the liquid in the evanescent field region with respect to the total volume.

$$V_{\text{total in the cube}} = V_t$$

$$V_{\text{total nanoparticles in the cube}} = V_n$$

$$V_{\text{total evanescent field regions in the cube}} = V_e$$

NPs Type	Silver			Gold		
NPs Diameter (nm)	20	40	60	20	40	60
$V_n$ (m <sup>3</sup> ) for 1 nanoparticle	$\sim 4.2 \times 10^{-24}$	$\sim 33.6 \times 10^{-24}$	$\sim 113.4 \times 10^{-24}$	$\sim 4.2 \times 10^{-24}$	$\sim 33.6 \times 10^{-24}$	$\sim 113.4 \times 10^{-24}$
$V_e$ (m <sup>3</sup> ) for 1 nanoparticle	$\sim 29.4 \times 10^{-24}$	$\sim 79.8 \times 10^{-24}$	$\sim 155.4 \times 10^{-24}$	$\sim 29.4 \times 10^{-24}$	$\sim 79.8 \times 10^{-24}$	$\sim 155.4 \times 10^{-24}$
$V_t$ (m <sup>3</sup> ) for 1 nanoparticle	$\sim 2.86 \times 10^{-17}$	$\sim 2.22 \times 10^{-16}$	$\sim 7.68 \times 10^{-16}$	$\sim 2.86 \times 10^{-18}$	$\sim 2.21 \times 10^{-17}$	$\sim 7.67 \times 10^{-17}$
$\frac{V_n}{V_t} \times 100$	$\sim 14.68 \times 10^{-6} \%$	$\sim 15.13 \times 10^{-6} \%$	$\sim 14.76 \times 10^{-6} \%$	$\sim 14.68 \times 10^{-5} \%$	$\sim 15.11 \times 10^{-5} \%$	$\sim 17.78 \times 10^{-5} \%$
$\frac{V_e}{V_t} \times 100$	$\sim 10.28 \times 10^{-5} \%$	$\sim 39.95 \times 10^{-6} \%$	$\sim 20.23 \times 10^{-6} \%$	$\sim 10.28 \times 10^{-4} \%$	$\sim 36.11 \times 10^{-5} \%$	$\sim 20.03 \times 10^{-5} \%$

Table 6: The approximate percentage of the nanoparticles fraction and the evanescence field around them

In conclusion, the volume of the nanoparticles and the of the evanescent field region around them as a percentage of the total liquid volume has been estimated. The calculation includes the following:

1. Nanoparticles are completely sphere;
2. The distance between each two is much more than the 20 nm ( $\times 2$  of the evanescent field) so that, for example they do not aggregate.
3. The evanescent field region around a nanoparticle is assumed to extend to 10 nm beyond the surface of the sphere.

### 8.3 Approaches and results

The setup in this section is similar to that shown in Figure 1. The difference is the camera which is employed to do the test (the first previous camera was not available); and because of that, the first thing done before using the nanoparticles was to find the limit of detection for the new camera. To do this, different concentrations of luminol in 3 different flow rates selected from the low range of velocity (see section 6.1) were mixed inside the channel. Using the same analysing scheme explained in Figure 28, the limit of detection, using 3 standard deviations (standard value defined by International Union of Pure and Applied Chemistry (IUPAC)) is measured as its being shown in Figure 46. The limit of detection is  $< 110 \mu\text{g/ml}$ . This value is more than the limit of detection for the chemiluminescence determined in section 7.1.1 and that is mainly because of the higher sensitivity of the camera used in that section.

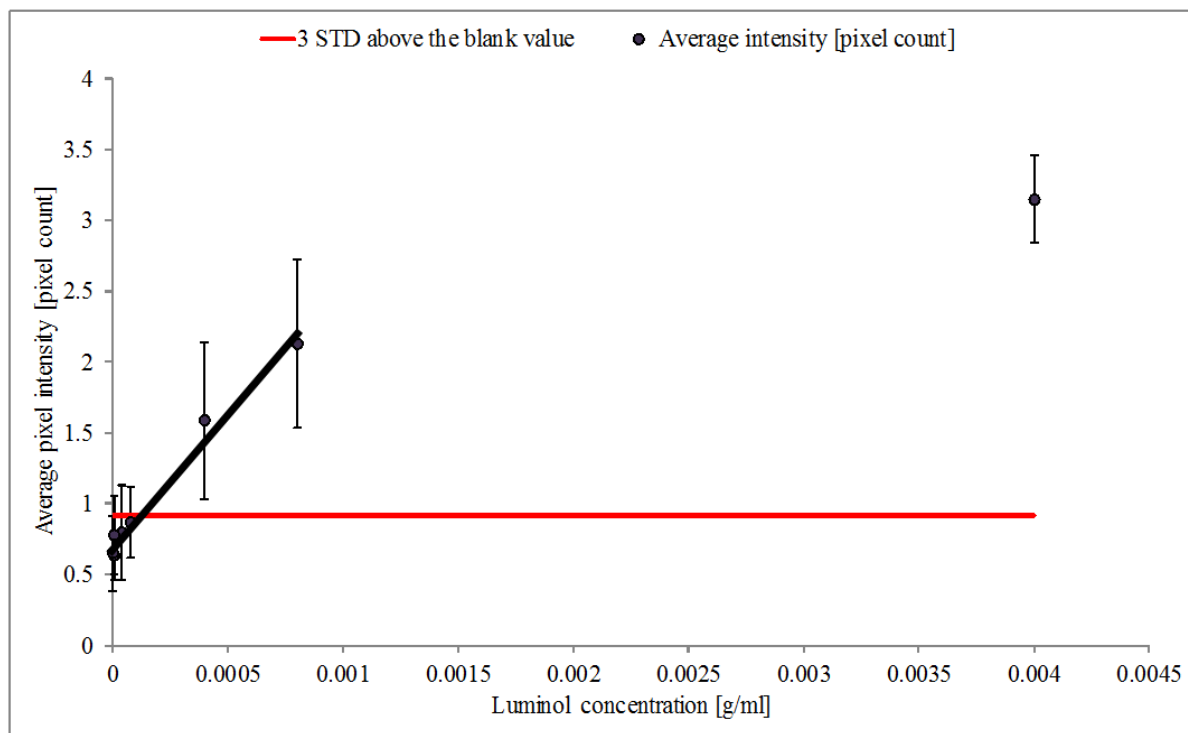


Figure 46: Average intensity over the different concentration of luminol to find limit of detection

Finding limit of detection, the objective of the next step is testing the enhancement of nanoparticles. To do that, each different size of silver and gold nanoparticles mixed separately in the luminol solution and pumped into the channel in three flow rates (results are shown in Table 7). The concentration chosen for this test is  $40 \mu\text{g/ml}$ , which is less than limit of detection that is determined before. To do the test,  $100 \mu\text{l}$  of nanoparticles added to  $100 \mu\text{l}$  of the luminol selected concentration (half each that divided the whole concentration of the luminol to half, which is  $20 \mu\text{g/ml}$ ).

In Table 7, its notable that the fourth column shows the ratio of the average pixel intensities with and without the nanoparticles, which is luminol diluted in distilled (DI) water (shown in column 3), the seventh column is the ratio of the calculated in column four but scaled by the difference in nanoparticles number density, which is always ten times higher for gold than silver in the same type and the same flow rates.

Flow rate = 0.15 $\mu\text{l/s}$	NPs Type	Average intensity [pixel count]	Enhancement ratio over water	Concentration [ $\text{m}^{-3}$ ]	Decay Time [s]	NP/DI
	20 nm Au	6.79830721	2.791859037	7.00E+17	85	2.791859037
	20 nm Ag	6.819666166	2.800630514	7.00E+16	88	28.00630514
	DI water	2.435046727			115	
	40 nm Au	5.901714371	2.423655491	9.00E+16	91	2.423655491
	40 nm Ag	6.540577857	2.686017391	9.00E+15	80	26.86017391
	DI water	2.435046727			115	
	60nm Au	6.12637261	2.515915831	2.60E+16	76	2.515915831
	60nm Ag	6.804203688	2.794280542	2.60E+15	38	27.94280542
	DI water	2.435046727			115	
Flow rate = 0.25 $\mu\text{l/s}$	NPs Type	Average intensity [pixels count]	Enhancement ratio over water	Concentration [ $\text{m}^{-3}$ ]	Decay Time [s]	NP/DI
	20 nm Au	4.290880544	2.236601479	7.00E+17	70	2.236601479
	20 nm Ag	4.623174329	2.409808065	7.00E+16	69	24.09808065
	DI water	1.918482387			81	
	40 nm Au	3.149667889	1.641749703	9.00E+16	70	1.641749703
	40 nm Ag	4.214858547	2.196975368	9.00E+15	58	21.96975368
	DI water	1.918482387			81	
	60 nm Au	3.462110137	1.804608768	2.60E+16	74	1.804608768
	60 nm Ag	4.7565737	2.479341866	2.60E+15	63	24.79341866
	DI water	1.918482387			81	
Flow rate = 0.35 $\mu\text{l/s}$	NPs Type	Average intensity [pixels count]	Enhancement ratio over water	Concentration [ $\text{m}^{-3}$ ]	Decay Time [s]	NP/DI
	20 nm Au	7.125373243	2.775021324	7.00E+17	80	2.775021324
	20 nm Ag	7.089404154	2.761012936	7.00E+16	64	27.61012936
	DI water	2.567682339			119	
	40 nm Au	7.082020147	2.758137188	9.00E+16	58	2.758137188
	40 nm Ag	7.587641251	2.9550545	9.00E+15	57	29.550545
	DI water	2.567682339			119	
	60 nm Au	7.41989243	2.889723669	2.60E+16	80	2.889723669
	60 nm Ag	7.685979118	2.9933528	2.60E+15	36	29.933528
	DI water	2.567682339			119	

Table 7: Average intensity in different flow rates and different nanoparticles and different decay time

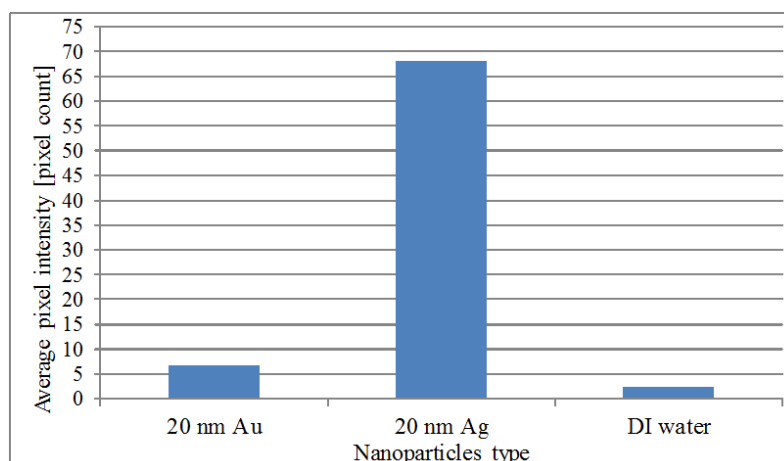


Figure 47: The average pixel intensity of chemiluminescence without nanoparticles (DI water) and with nanoparticles (20 nm Au and Ag)

Figure 47 shows the average pixel intensity with and without nanoparticles by considering the different concentrations of the gold and silver nanoparticles (“the silver nanoparticles concentration < the gold nanoparticles concentration” by taking to account silver and gold mass into account with the factor of 10). Multiplying this difference to the enhancement ratio of the silver, this value is changed to the value of  $\sim 28$ . This difference is between same sizes of nanoparticles.

In conclusion, limit of detection is determined as  $< 110 \mu\text{g/ml}$ . A set of test including 3 different flow rates is done and the average intensity of the light inside the whole channel including the decay time of the chemiluminescent light is measured. As it is shown in Figure 47 briefly, nanoparticles increase the intensity of the light and this is discussed in the next section.

### 8.4 Discussion

Table 7 shows nanoparticles enhance collected light intensity coming from the chemical reaction (CL). Considering the number density of nanoparticles, silver gives a greater enhancement than gold per nanoparticle.

The Jablonski diagram shown in Figure 4 shows the lifetime of the emitted light in the way that an electron which goes to a higher excited level of energy takes more time to come back to the ground state and emit light. Hence, the lifetime of the chemiluminescence with nanoparticles decreased compare to without nanoparticles. This is what has happened and shown in the results that the chemiluminescence light has shorter lifetime with nanoparticles compare to without nanoparticles. The results show that nanoparticles enhance the intensity of the light; since energy is a conservative parameter and no other external source of energy is present, there should be something else that decreases. The intensity of the initial emission (chemiluminescence without nanoparticles) increases.

Figure 47 shows that for a flow rate such as  $0.15 \mu\text{l/s}$ , there is a distinguishable difference between different sizes of the same type of nanoparticles.

The origin of the enhancement is unknown but could include:

## Nanoparticle enhancement of chemiluminescence

- i. Plasmonic effect
- ii. Catalytic effect
- iii. Lateral motion effect

The mechanism of the enhancement cannot be uniquely determined from these results. It could be an optical effect such as plasmonic enhancement. It could be that the majority of the nanoparticles are flowing down the centre of the channel back towards the camera. Intensity enhancement could also be a chemical effect, where the nanoparticles could behave as a catalyst and increase the rate of reaction between luminol and sodium hydroxide [46]. Alternatively it could be a fluidic effect where lateral motion of the nanoparticles could increase diffusive mixing. There is a hypothesis that the reflection of the nanoparticles passing in the liquid could be another reason of having the enhancement but the symmetry of the system decrease its possibility cause the same effect could be in all directions not just the direction of the detection.

In conclusion, after finding the limit of detection  $< 110 \mu\text{g/ml}$  for the setup, the experiment is repeated using nanoparticles and the intensity increased. As an example in the flow rate of  $0.15 \mu\text{l/s}$  and the concentration of  $20 \mu\text{g/ml}$ , the intensity of the light using 20 nm silver nanoparticles enhanced by a factor of 30-fold. Also, increasing the flow rate increased the intensity of the chemiluminescence with nanoparticles.

Further work is required to understand the physical principles behind this providing observation on enhancement.

## 9 Conclusion

The aim of the project was to design and fabricate a microfluidic device; to characterise chemiluminescence inside it and quantitatively analyse images of chemiluminescence flow. The effects of changing the flow rate and reagent concentration were also investigated. Detection limit of luminol for the optical system determined as  $< 40 \text{ ng/ml}$ . The effect of increasing the flow rate on the intensity of the light is investigated. The resultant light intensity through the channel increased by adding luminol and with increasing flow rate. Increased flow rate also decreased the rate of the decay and the decay length of the emitted light.

The detection limit of the luminol for the correspondent new optical system for nanoparticles determined as  $< 110 \text{ }\mu\text{g/ml}$ ; and the intensity enhanced with the aim of improving the limit of detection using silver and gold nanoparticles. The mechanism of the enhancement was suggested to be due to surface plasmon effect but could not be conclusively demonstrated and that's because of the calculation made in section 8.2 that shown that this enhancement couldn't just be the surface plasmons.

## 10 Future work

Rapid prototyping technology (3D-printing) is one of the interesting ways of making a mould for fabricating a chip for this project. Although its quick but there are still limitations such as lack of surface smoothness. Alternatively, photolithography would provide flatter and smoother surfaces.

Another limitation of the experiments in this project was the reaction between luminol and PDMS. Future work could be including improving chemical capability. Furthermore, designing a longer channel will let the researchers have more data to analyse the effect of changing the flow rate on the decaying length of the light. In terms of the fabrication and also layout of the chips some of the useful modifications could be made on the device such as designing a separate inlet for pumping nanoparticles and also splitting the device to two sections: “light source”, where the chemicals mix to produce light and “optical amplifier”, where nanoparticles would be added with the purpose of increasing the light intensity. The layouts of some of these designs are shown in Figure 48 and their fabricated channels are shown in Figure 15.

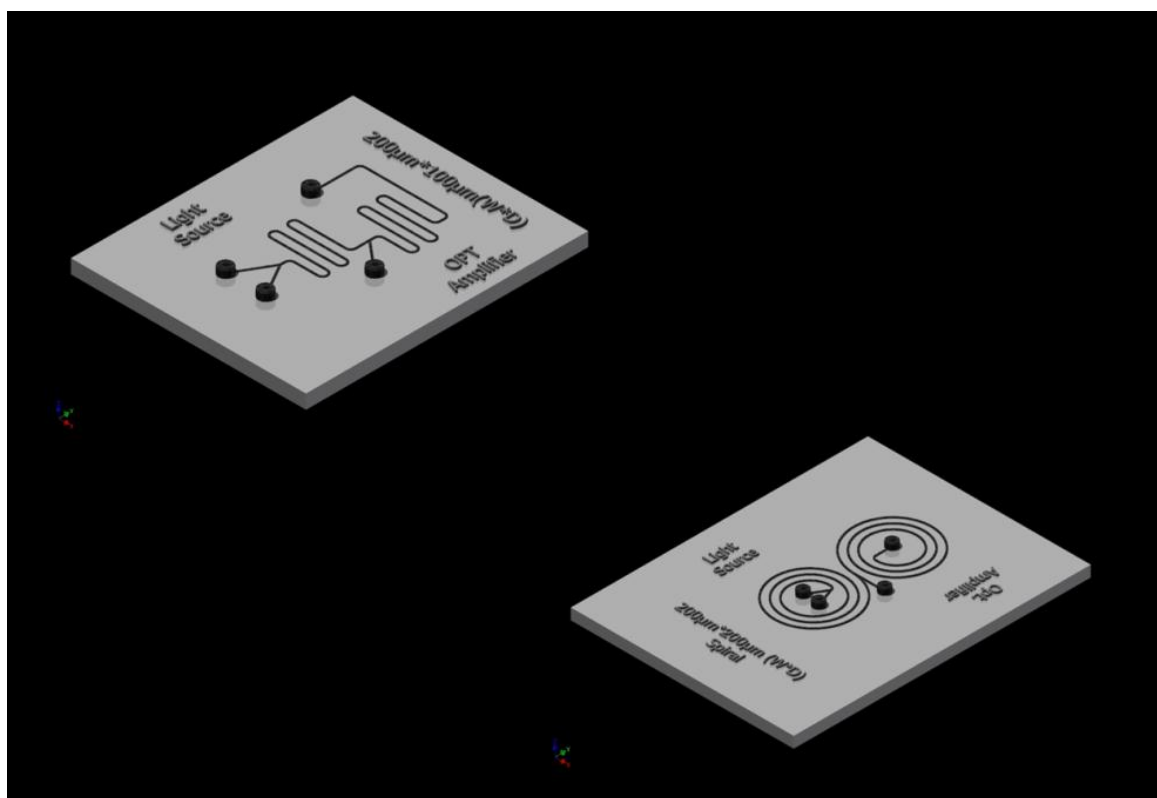


Figure 48: Future device layouts including "light source" and "optical amplifier" parts

One of the important objectives as the future work is to understand of where the enhancement comes from. In another word, to do an experiment of finding limit of detection using nanoparticles with different concentrations of luminol to make sure that the enhancement has not increased the noise ratio the same amount. The catalytic behaviour of the nanoparticles should be studied such as the effect of the shape of nanoparticles and also the reaction between different chemicals in the mixture individually and together on the nanoparticles.



## Future work

The more accurate evanescent field value should be calculated. The reflection effect of the nanoparticles should be checked by putting detector in different angles around the channel to check the intensity.

On the other hand, as mentioned at the beginning of this project, one of the useful applications of this characterised device is that, it provides a platform for performing bioluminescence and testing DNA, bacteria and also proteins such as aequorin in detecting the amount of calcium ions.

## 11 Reference

- [1] O. Shimomura, F. H. Johnson, and Y. Saiga, "Extraction, Purification and Properties of Aequorin, a Bioluminescent Protein from the Luminous Hydromedusan, Aequorea," *Journal of Cellular and Comparative Physiology*, vol. 59, no. 3, pp. 223–239, Jun. 1962.
- [2] O. Reynolds, "An Experimental Investigation of the Circumstances which determine whether the Motion of Water shall be Direct or Sinusous, and of the Law of Resistance in Parallel Channels," *Society, The Royal Transactions, Philosophical Society, Royal*, vol. 174, no. May, pp. 935–982, 2013.
- [3] N.-T. Nguyen and S. T. Wereley, *Fundamentals and Applications of Microfluidics (Integrated Microsystems)*. Artech House, 2006, p. 514.
- [4] F. A. Morrison, *An Introduction to Fluid Mechanics*, 1st Editio. New York: Cambridge University Press, 2013, p. 960.
- [5] K. Wyka, W. Clark, and P. Mathews, *Foundations of Respiratory Care*, 2nd editio. Delmar Cengage Learning, 2011, p. 1152.
- [6] M. G. Lee, S. Choi, and J.-K. Park, "Three-dimensional hydrodynamic focusing with a single sheath flow in a single-layer microfluidic device.," *Lab on a chip*, vol. 9, no. 21, pp. 3155–60, Nov. 2009.
- [7] V. Hessel, H. Löwe, and F. Schönfeld, "Micromixers—a review on passive and active mixing principles," *Chemical Engineering Science*, vol. 60, no. 8–9, pp. 2479–2501, Apr. 2005.
- [8] a G. Hadd, D. E. Raymond, J. W. Halliwell, S. C. Jacobson, and J. M. Ramsey, "Microchip device for performing enzyme assays.," *Analytical chemistry*, vol. 69, no. 17, pp. 3407–12, Sep. 1997.
- [9] H. Search, C. Journals, A. Contact, M. Iopscience, and I. P. Address, "Characterization method for a new diffusion mixer applicable in micro flow injection analysis systems," vol. 199, pp. 2–6, 1999.
- [10] a E. Kamholz, B. H. Weigl, B. a Finlayson, and P. Yager, "Quantitative analysis of molecular interaction in a microfluidic channel: the T-sensor.," *Analytical chemistry*, vol. 71, no. 23, pp. 5340–7, Dec. 1999.
- [11] M. Al-Rawashdeh, F. Yu, T. a. Nijhuis, E. V. Rebrov, V. Hessel, and J. C. Schouten, "Numbered-up gas–liquid micro/milli channels reactor with modular flow distributor," *Chemical Engineering Journal*, vol. 207–208, pp. 645–655, Oct. 2012.
- [12] R. F. Ismagilov, A. D. Stroock, P. J. A. Kenis, G. Whitesides, and H. A. Stone, "Experimental and theoretical scaling laws for transverse diffusive broadening in two-phase laminar flows in microchannels," *Applied Physics Letters*, vol. 76, no. 17, p. 2376, 2000.

## Reference

- [13] Z. Wu and N.-T. Nguyen, "Convective–diffusive transport in parallel lamination micromixers," *Microfluidics and Nanofluidics*, vol. 1, no. 3, pp. 208–217, Nov. 2004.
- [14] L. Wang, D. Liu, X. Wang, and X. Han, "Mixing enhancement of novel passive microfluidic mixers with cylindrical grooves," *Chemical Engineering Science*, vol. 81, pp. 157–163, Oct. 2012.
- [15] S. Hossain, M. a. Ansari, and K.-Y. Kim, "Evaluation of the mixing performance of three passive micromixers," *Chemical Engineering Journal*, vol. 150, no. 2–3, pp. 492–501, Aug. 2009.
- [16] H. Wang, P. Iovenitti, E. Harvey, and S. Masood, "Optimizing layout of obstacles for enhanced mixing in microchannels," *Smart Materials and Structures*, vol. 11, no. 5, pp. 662–667, Oct. 2002.
- [17] K. Hosokawa, T. Fujii, and I. Endo, "Droplet-based nano/picoliter mixer using hydrophobic microcapillary vent," *Micro Electro Mechanical ...*, pp. 388 – 393, 1999.
- [18] P. Paik, V. K. Pamula, and R. B. Fair, "Rapid droplet mixers for digital microfluidic systems.," *Lab on a chip*, vol. 3, no. 4, pp. 253–9, Nov. 2003.
- [19] M. D. Furtaw, D. Lin, L. Wu, and J. P. Anderson, "Near-Infrared Metal-Enhanced Fluorescence Using a Liquid–Liquid Droplet Micromixer in a Disposable Poly(Methyl Methacrylate) Microchip," *Plasmonics*, vol. 4, no. 4, pp. 273–280, Sep. 2009.
- [20] Z.-X. Guo, Q. Zeng, M. Zhang, L.-Y. Hong, Y.-F. Zhao, W. Liu, S.-S. Guo, and X.-Z. Zhao, "Valve-based microfluidic droplet micromixer and mercury (II) ion detection," *Sensors and Actuators A: Physical*, vol. 172, no. 2, pp. 546–551, Dec. 2011.
- [21] K.-Y. Tung, C.-C. Li, and J.-T. Yang, "Mixing and hydrodynamic analysis of a droplet in a planar serpentine micromixer," *Microfluidics and Nanofluidics*, vol. 7, no. 4, pp. 545–557, Feb. 2009.
- [22] M. Campisi, D. Accoto, F. Damiani, and P. Dario, "A soft-lithographed chaotic electrokinetic micromixer for efficient chemical reactions in lab-on-chips," *Journal of Micro-Nano Mechatronics*, vol. 5, no. 3–4, pp. 69–76, Feb. 2010.
- [23] B. Xu, T. N. Wong, N.-T. Nguyen, Z. Che, and J. C. K. Chai, "Thermal mixing of two miscible fluids in a T-shaped microchannel.," *Biomicrofluidics*, vol. 4, no. 4, p. 44102, Jan. 2010.
- [24] R. Karl Michael Landshoff, Ed., *Magnetohydrodynamics: A Symposium [held at Palo Alto, Cal.]*. USA: Stanford University Press, 1957, p. 115.
- [25] Y. Wang, J. Zhe, B. T. F. Chung, and P. Dutta, "A rapid magnetic particle driven micromixer," *Microfluidics and Nanofluidics*, vol. 4, no. 5, pp. 375–389, Jun. 2007.
- [26] N.-T. Nguyen and Z. Wu, "Micromixers—a review," *Journal of Micromechanics and Microengineering*, vol. 15, no. 2, pp. R1–R16, Feb. 2005.

## Reference

- [27] Y. Lin, G. J. Gerfen, D. L. Rousseau, and S.-R. Yeh, "Ultrafast microfluidic mixer and freeze-quenching device.," *Analytical chemistry*, vol. 75, no. 20, pp. 5381–6, Oct. 2003.
- [28] J. E. House, *Fundamentals of Quantum Chemistry (Complementary Science)*. Academic Press, 2003, p. 312.
- [29] A. M. Garcia-Campana, *Chemiluminescence in Analytical Chemistry*. CRC Press, 2001, p. 640.
- [30] Y.-X. Guan, Z.-R. Xu, J. Dai, and Z.-L. Fang, "The use of a micropump based on capillary and evaporation effects in a microfluidic flow injection chemiluminescence system.," *Talanta*, vol. 68, no. 4, pp. 1384–9, Feb. 2006.
- [31] S. Bhattacharya, a. Datta, J. M. Berg, and S. Gangopadhyay, "Studies on surface wettability of poly(dimethyl) siloxane (PDMS) and glass under oxygen-plasma treatment and correlation with bond strength," *Journal of Microelectromechanical Systems*, vol. 14, no. 3, pp. 590–597, Jun. 2005.
- [32] P. Taylor, M. J. Owen, and P. J. Smith, "Journal of Adhesion Science and Plasma treatment of polydimethylsiloxane," no. March 2013, pp. 37–41, 2012.
- [33] B. F. P. Bretherton, "The motion of rigid particles i n a shear flow at low Reynolds number," no. 1956, 1962.
- [34] C. C. Demonstrations, "oxidation of luminol," *The royal society of chemistry*, pp. 12–13.
- [35] D. Fleming, "The Chemiluminescence of Luminol - Home," *University of Bristol*. [Online]. Available: <http://www.chm.bris.ac.uk/webprojects2002/fleming/mechanism.htm>. [Accessed: 30-May-2013].
- [36] E. Wurrbergt, "Luminol and Related Compounds under Electron-Beam Excitation. Enhancement of Light Yields by Addition," vol. 83, no. 21, pp. 2692–2696, 1979.
- [37] J. Holman, *Experimental Methods for Engineers (McGraw-Hill Mechanical Engineering)*. McGraw-Hill Science/Engineering/Math, 2000, p. 720.
- [38] D. He, Z. Zhang, Y. Huang, and Y. Hu, "Chemiluminescence microflow injection analysis system on a chip for the determination of nitrite in food," *Food Chemistry*, vol. 101, no. 2, pp. 667–672, Jan. 2007.
- [39] M. H. Chowdhury, K. Aslan, S. N. Malyn, J. R. Lakowicz, and C. D. Geddes, "Metal-enhanced chemiluminescence.," *Journal of fluorescence*, vol. 16, no. 3, pp. 295–9, May 2006.
- [40] S. N. Malyn, "Metal-enhanced chemiluminescence: radiating plasmons generated from chemically induced electronic excited states," vol. 88, no. 17, pp. 1–8, 2009.

## Reference

- [41] S. Jockusch, "Surface Plasmons Literature Listing," 2007. [Online]. Available: <http://turroserver.chem.columbia.edu/surfaceplasmons/>. [Accessed: 19-May-2013].
- [42] G. Sun and J. B. Khurgin, "Plasmon Enhancement of Luminescence by Metal Nanoparticles," *IEEE Journal of Selected Topics in Quantum Electronics*, vol. 17, no. 1, pp. 110–118, Jan. 2011.
- [43] N. Savage, "Scientists Measure Oscillations in Visible Light Pulses | SPIE Newsroom: SPIE," *SPIE*, 2004. [Online]. Available: <http://spie.org/x16147.xml>. [Accessed: 19-May-2013].
- [44] M. H. Chowdhury, K. Aslan, S. N. Malyn, J. R. Lakowicz, and C. D. Geddes, "Metal-enhanced chemiluminescence: Radiating plasmons generated from chemically induced electronic excited states.," *Applied physics letters*, vol. 88, no. 17, p. 173104, Apr. 2006.
- [45] K. Aslan and C. D. Geddes, "Metal-enhanced chemiluminescence: advanced chemiluminescence concepts for the 21st century.," *Chemical Society reviews*, vol. 38, no. 9, pp. 2556–64, Sep. 2009.
- [46] S. U. Abideen, "Chemiluminescent Reactions Catalyzed by Nanoparticles of Gold, Silver, and Gold/Silver Alloys - viewcontent.cgi," *MASTER OF SCIENCE*, p. 57, 2012.